ALMA MATER STUDIORUM
UNIVERSITÀ DI BOLOGNA

Department of industrial engineering

Master's Degree in Aerospace Engineering

Class LM-20

Develpment and testing of a test bench for the analysis of plasma actuators at high-Reynolds numbers

Dissertation in:
Experimental Methods in Aerodynamics

Supervisor
Prof. Gabriele Bellani

Co-Supervisor
Dr. Lorenzo Magnani

Defended by
Brian Sebastiani

Academic Year 2024/2025
Graduation Session 24^{th} March 2026

Contents

List of Figures

List of Tables

List of Symbols

a	Speed of sound
A	Cross-section's area
b	Dielectric thickness
B	Log law constant
C	Number of particles per volume
C_M	Capacitance
c_f	Skin friction coefficient
d	Displacement magnitude
d_{diff}	Diffraction contribution to particle effective diameter
d_{gap}	Electrodes' gap
d_p	Diameter of particles used for flow visualization
d_τ	Effective particle diameter
D	Hydraulic diamter
D_a	Aperture diameter
D_x, D_y	Side lengths of the interrogation area
$\vec{E}$	Electric field
f	Focal length
f_{AC}, f	AC frequency
f_w	Law of the wall
f'_w	Derivative of the law of the wall
$\vec{f}_i$	Body force per unit of power
F_D	Velocity defect law
F_I	Particle loss due to in-plane motion
F_O	Particle loss due to out-of-plane motion
F_Δ	Particles matching loss due to displacement gradients
g	Gravitational acceleration magnitude
g_e	Gap between ground and exposed electrode (stair-shaped configuration)
h	Channel height
h_e	Contraction exit's height
h_i	Contraction inlet's height
I	Discharge current
$I(x, y)$	Light intensity map of the first image
$I'(x, y)$	Light intensity map of the second image
$I_M(t)$	Displacement current in the capacitor
k	Von Kàrmàn constant
K	Pressure loss coefficient

l_c	Contraction's length
L	Length scale
L	Channel length
m	Interrogation area's width
M	Mach number
M	Magnification
n	Interrogation area's height
n_c	Number of cycles
n_e	Negative ions density
n_i	Positive ions density
N_I	Avarage number of particles per interrogation area
p	Pressure
p_{amb}	Ambient temperature
p_{static}	Static pressure
p_{total}	Total pressure
p_w	Pressure at wall position
p_x	Pixel size
$P(t)$	Istantaneous power consumed
P_{av}	Avarage power consumed per cycle
P_d	Dissipated power
Q	Flow rate
$Q_M(t)$	Istantaneous charge accumulated in the capacitor
R	Shunt resistance
$R(x, y)$	Cross-correlation map
Re	Reynolds number
Re	Bulk Reynolds number
Re_D	Reynolds number defined with the hydraulic diameter
Re_0	Reynolds number defined with centerline velocity of the channel flow
Re_τ	Friction Reynolds number
St	Strouhal number
Δt	Interframe time
T	Period of AC cycle
T_{amb}	Ambient temperature
u	x-component of velocity fluctuations
u_{rms}	Root mean square of x-component of velocity fluctuations
u_τ	Wall region's velocity scale
$\mathbf{u}$	Velocity fluctuations' vector
U	x-component velocity vector
U_0	Centerline avarage axial component of velocity in the channel flow
U_p	Particle velocity
$\bar{U}$	Bulk velocity
$\mathbf{U}$	Velocity vector
v	y-component of velocity fluctuations
v_{rms}	Root mean square of y-component of velocity fluctuations
V_a	Voltage applied to the the plasma actuator

V_{AC}	AC voltage
V_{ionic}	Ionic wind's velocity magnitude
V_{p-p}	Peak to peak voltage
$V_R(t)$	Shunt resistor voltage
$V_M(t)$	Capacitor's voltage
w	Channel width
w_{ce}	Width of the grounded electrode (stair-shaped configuration)
w_{rms}	Root mean square of z-component of velocity fluctuations
W	z-component of velocity vector
W_k	Kinetic power
W_E	Electrical power
y^+	Wall distance in inner units
z	Piezometric height
β	Medium porosity
δ	Half channel's height
δ_1^*	Displacement thickness
δ_ν	Wall region's length scale
δz_0	Laser sheet thickness
Δ	Avarage displacement
ϵ	Dielectric coefficient
ϵ	Surface roughness
η_k	Electro-kinetic conversion efficiency
λ	Laser wavelength
μ	Dynamic viscosity of a generic fluid
ν	Kinematic viscosity of a generic fluid
ρ	Fluid's density
ρ_p	Density of particles used in flow visualization
$\tau(y)$	Total shear stress
τ_p	Particles' time constant (tracer dynamcis)
τ_w	Total shear stress at the wall
Φ	Non-dimensional function (Law of the wall)

Abstract

Controlling flows at high Reynolds numbers has many important practical applications, for example drag reduction of vehicles. Indeed, minimizing drag is one of the main strategies for reducing fuel consumptions and decreasing emissions of polluting agents and greenhouse effect gases, like CO_2.

The complexity of high Reynolds number flows dynamics, poses challenging problems when designing efficient and reliable control strategies. In order to do so, the flow control device itself, should be capable of dynamically adapting its response to changing conditions. Among the active flow control devices, plasma actuators, thanks to their unique characteristics, are one of the best candidate for this scope.

This thesis has the objective of developing and testing a specific test bench for the analysis and study of plasma actuators for active flow control at high Reynolds numbers.

Keywords: Plasma actutors, active flow control, high Reynolds number flows

Chapter 1

Introduction

Flow control is one of the main research topic in aerodynamics. The words, flow control, collect a wide range of applications. Mitigation of boundary layer separation, reduction of flow instabilities, turbulence reduction and even the opposite effects, as well as aerodynamic control for flying vehicles. In particular drag reduction, which is the key point for reducing consupmtions, has brought researchers to develop several strategies to achieve this goal.

Flow control devices can be divided into two families:

- **Passive**: the effect on the flow is obtained without energy input;
- **Active**: energy must be provided to the device to induce an effect on the flow;

Passive devices, such as riblets, demonstrated to be an efficient way of decreasing drag only at particular flow conditions, and indeed this is the main problem of this category, i.e. they cannot adapt their response to changing conditions, but for example vortex generators for mitigation of boundary layer separation are still widely used because the overall benefits are higher with respect to reduction of aerodynamic efficiency.

By definition, active devices can adapt their response in time; the drawback is that to do so they require energy. Moreover, it must be underlined that their response, not always can be the result of an event happened in flow. Except for boundary layers separation, flow instabilities and turbulence are difficult to control because the flow dynamics is too complex to be controlled effectively in certain conditions, and still do not exist efficient and reliable actuation modes. Among active devices for flow control there are plasma actuators.

Plasma actuators have been developed in different shapes and with different functions, but they are all united by the fact that the working principle is based on the ionization of the fluid to be controlled, and the time response is among the fastest within active devices. This makes them one of the best candidates especially for high Reynolds number flows where flow dynamics is characterized by a wide range of frequencies.

1.1 Thesis objectives and outline

This thesis project has the aim of developing a test bench for fully characterizing the behaviour of a generic plasma actuator, both with flow and electrical measurements. In this way, low to moderate Reynolds number tests can be safely performed in a controlled environment. With data obtained, optimization of the actuator geometry and efficiency can be easily carried out. Objectives, of the performed analyses, are: first, characterizing the behaviour of the wind tunnel and verifying if it is compliant with the design specifications and secondly, performing a first trial with active actuator in order to simulate a real condition of usage.

So, after designing the platform, the full set-up has been built and tested in order to validate the system.

The present work explains all the design choices taken to develop the final set-up layout, considering the requirements related to plasma actuators usage, together with the experimental results obtained. To summarize, the thesis is divided into:

- **Chapter 2**: theoretical background divided into: description of plasma actuators working principle, categories and applications, then, the second part is about theory on wall bounded flows, in particular fully developed channel flow;
- **Chapter 3**: description of the test bench design; after a brief overview on the theoretical basis of wind tunnels, design choices are presented and discussed in detail;
- **Chapter 4**: in the first part, flow measurement limitations related to plasma actuators are explained and theoretical background about the selected technique is given; the second part instead, is focused on electrical measurement related to techniques for plasma actuator's power estimation;
- **Chapter 5**: details about the implemented experimental set-up are given;
- **Chapter 6**: results of the wind tunnel characterization are presented and preliminary measurements of the mean velocity field with active plasma actuator are reported;
- **Chapter 7**: results presented in the previous chapter are discussed and analysed;
- **Chapter 8**: in the final chapter, conclusions about the results are given and future perspectives about following tests are presented.

Chapter 2

Theoretical background

2.1 Plasma actuators for flow control

Active flow control through plasma actuators is the only strategy that nowadays is capable of controlling flows without movable parts and without injection of mass into the base flow. These are the key characteristics of this technology. Moreover, the relative simplicity of the architecture and the possibility of scaling it with modern fabrication techniques allows to dramatically reduce the interference of the actuators with the flow.

Even if this device seems to be one of the best candidate for reaching outstanding and wide control capabilities for aerodynamic applications, as it will be explained in detail in the following sections, up to now there are still some issues which restrict usage to only experimental applications, in particular:

- control authority in complex flows conditions: in general air humidity, pressure, temperature and density, highly affect the actuators [26];
- actuator durability: especially the actuators with dielectric materials have limited lives due to the dielectric degradation;
- actuation management: the apparatus used for the actuation control must be capable of safely generating and handling high voltage input and a good control of the frequency and wave shape is required.

All these aspects must be taken into account when designing platforms to be implemented on manned flying vehicles. The requirements are generally less stringent for ground applications, such as flow control in pipes or heat exchangers, where actuator malfunctions do not pose severe safety risks but only lead to reduced performance. For indoor applications, ozone production during actuator usage must be carefully controlled by measuring its concentration.

2.1.1 Actuators' working principle

All this family of actuators is united by the generation of plasma by applying a strong electric field with two electrodes that ionizes air. The densities of negative and positive ions are almost equal since the reaction generates pairs of opposite charges. Moreover, since it is not possible to obtain a full ionization of the air volume within

the electrodes gaps, neutral species are present too. The charge balance is almost null, indeed the plasma is called quasi neutral [14]. So, the gas is not fully ionized and to initiate the process, a certain amount of free electrons is required. These electrons collide with neutrals and generate a cascade reaction that is sustained by a strong applied electric field. Pairs of positive and negative ions are produced and this is the so called Townsend discharge [26]. Ions feel the electric fields and drift towards the opposite charged electrode, driven by Coulomb force. No magnetic field is applied in general with these types of actuators and indeed Lorentz force is not used as control input.

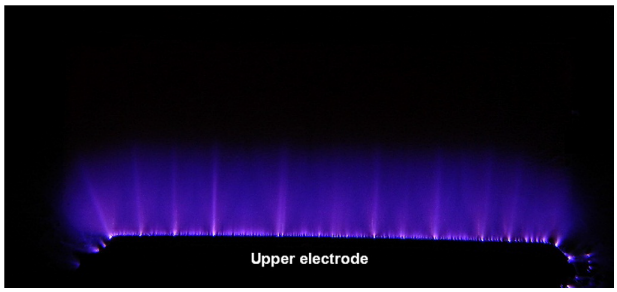

Figure 2.1: Glow discharge of a Dieletric Barrier Discharge actuator (taken from [15]).

In order to initiate the plasma, it is necessary to overcome the breakdown electric field E_b of the gas, which is the value needed to sustain the electron-ion pair generation in absence of space charge fields [14]. The temperature increase in the plasma region is limited and indeed this type of plasma is referred to as non-thermal [35]. The desired operational mode is the glow discharge, i.e. when the current density due to ions movement is independent on the current flowing in the circuit [14]. In the discharge it is always possible to distinguish the filamentary pattern that can be seen also in Fig.2.1. These brighter strips originate from propagation streamers that are local fast ionization regions [25]. This phenomenon depends on environmental conditions [25], actuator surfaces and materials [15] and actuation mode [25], i.e. input voltage amplitude and cycle shape. These conditions modify the charge distribution and by doing so, they alter the generation of a uniform discharge. Instead, the generation of electric arcs between electrodes must be avoided since has a detrimental effect on the actuator reducing its life.

2.1.2 Actuators' architectures

There are mainly three plasma actuator topologies [43]:

- Corona discharge;
- Spark-jet;
- Dielectric Barrier Discharge.

Even if plasma is generated in all of those, each category generates it with different strategies and in this way, it is possible to obtain similar or completely different effects on the flow. In the following sections these architectures will be presented along with applications examples.

2.1.2.1 Corona Discharge actuator

Historically, is the first architecture developed [26], and it is the simplest among these presented. Only two electrodes are required and usually a DC power source is applied. The input signal in the actuators is on the order 1 to 10 $kVolts$. One of the two electrodes must have or a needle shape or could be a wire; in any case it should have a small cross section in order to enhance the electric field and indeed this electrode acts as the source for the ionization. Two types of corona discharge are distinguished [26], [41]:

- **Positive corona**: has the positive poles in the needle electrode; photoionization in the air gap between the two electrodes frees electrons that migrate towards the positive poles whereas the positive ions move towards the grounded pole;
- **Negative corona**: opposite polarity with respect to positive corona, and in this case electrons are produced by the high voltage needle electrode.

In both cases, the ionization is sustained by the electrons avalanche and by the photoionization, indeed photons are emitted when ions recombine to form a neutral and this energy released can trigger the generation of other ions. The second electrode is in general a plate collocated at a certain distance from the first electrode. A typical layout is depicted in Fig.2.2.

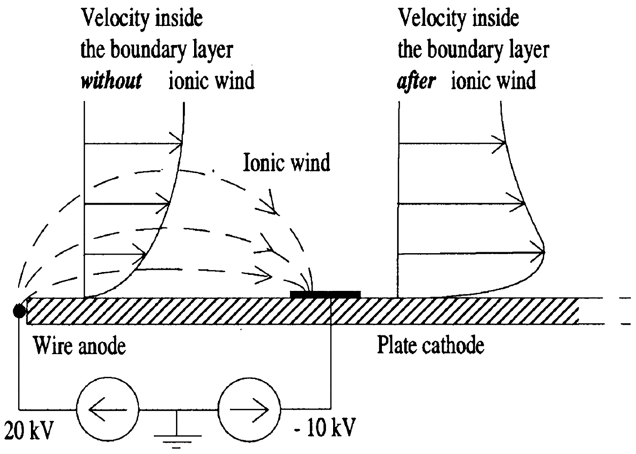

Figure 2.2: Surface Corona Discharge actuator (taken from [43]).

Coulomb force drives charges which collide with other particles, both ions and neutrals, and transfer their momentum. Thus, the so called ionic wind is generated and the flow speed V_{ionic} turns out to follow the law of Eq.(2.1) [41]:

$$V_{ionic} \propto \sqrt{I d_{gap}} \tag{2.1}$$

where I is the discharge current and d_{gap} is the distance between the two electrodes. In reality, this proportionality is verified only up to a certain threshold value of the current and, as the current increases, the V_{ionic} decreases as shown in Fig.2.3a. This behaviour is due to the reduction of the discharge gap, since the effective gap extends from the end of the corona region and in this area the high conductivity

of the plasma cancels out the applied electric field. Moreover, the discharge at the other electrode generates a flow in the opposite direction that lowers again the V_{ionic}. This saturation effect is particularly evident for the negative corona. Considering the spatial development of V_{ionic}, Fig.2.3b shows an exponential decrease in intensity as the distance from the corona increases.

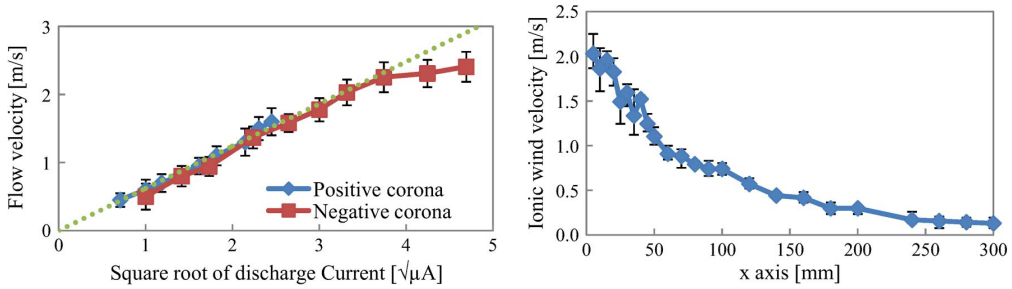

(a) (b)

Figure 2.3: V_{ionic} evolution as a function of the square root of the discharge current (a). V_{ionic} evolution as a function of the distance from the corona region (b) (taken from [41]).

In order to quantify the effectiveness of the actuator in generating momentum, it has been introduced the electro-kinetic conversion efficiency η_k expressed as [41]:

$$\eta_k = \frac{W_k}{W_E} x100[\%] \tag{2.2}$$

where W_k is the kinetic power injected by the actuator and W_E the electrical power used in the discharge. The values of η_k are in general as low as 0.1% and the maximum speed achievable is limited to values lower than 10 m/s in quiescent flow condition, due to saturation at high voltages [41], [24], [26]. Moreover, as the external free stream velocity increases, also the discharge current increases [26]. It is also important to underline that the negative corona produces ten times the ozone produced by the positive corona at the same conditions of power and geometry of the actuator [41].

2.1.2.2 Spark-jet

Spark-jet actuators are mainly used to generate synthetic jets [43]. The structure is generally an empty cylinder made of insulating material with a small orifice on the side exposed to the flow. Inside, there are arranged: an anode electrode, a cathode electrode and a grid electrode. The working principle follows three stages: energy deposition when the discharge goes from the cathode to the grid and the anode heats up the gas then, high temperature and pressure gas exits from the orifice to form the jet and finally, the chamber cools down rapidly, fresh air fills again the chamber and the process could repeat again. Recently, an additional trigger electrode demonstrated to enhance the energy deposition. Fig.2.4 illustrates this architecture.

The peak speed of the jet core is between 230 m/s [43] and 310 m/s [42] and decreases in time as the chamber loses the gas. After 600 μs the jet velocity reaches

a plateau [43].

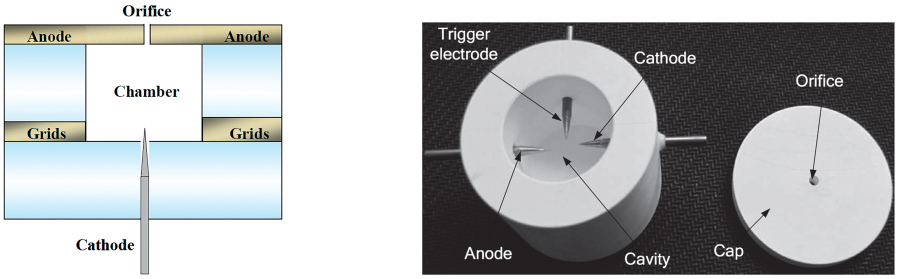

(a) (b)

Figure 2.4: Architecture of spark jet actuator lateral view (a). Opened actuator with the trigger electrode (b) (taken from [43]).

2.1.2.3 Dielectric barrier discharge

Dielectric barrier discharge (DBD) actuators are the most widely used among the plasma actuators applied for flow control and they can be considered the evolution of the corona discharge. The common architecture consists of one electrode exposed to the flow while the other is covered with a dielectric material and insulated, as shown in Fig.2.5. DBD actuators have a better resistance to glow to arc transition since on the dielectric establish a charge accumulation that reduces the electric field and quenches the discharge.

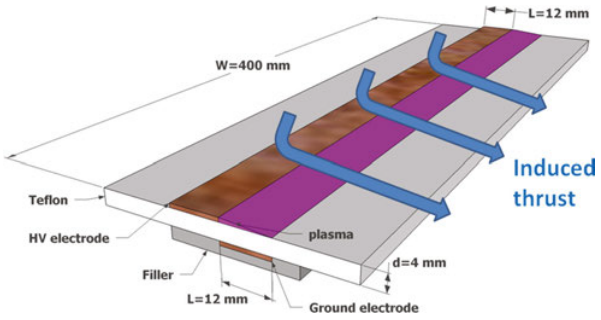

Figure 2.5: Typical DBD actuator architecture (taken from [35]).

Basically the structure can be compared to a capacitor and during usage no DC current flows in the circuit but only displacement current is allowed [26]. Indeed the DBD actuator can not operate in DC mode since the charge accumulation on the dielectric blocks the actuation. As well as the corona actuator, the body force per unit of volume $\vec{f_i}$ generated can be expressed as [35]:

$$\vec{f_i} = (n_i - n_e)\vec{E} \tag{2.3}$$

where n_i and n_e are the positive ions and electrons number densities respectively and $\vec{E}$, is the electric vector field . During one phase of the AC cycle, electrons leave the exposed electrode and deposit on the dielectric while on the other half, electrons flow from the dielectric in the opposite direction towards the exposed electrode [14], [17].

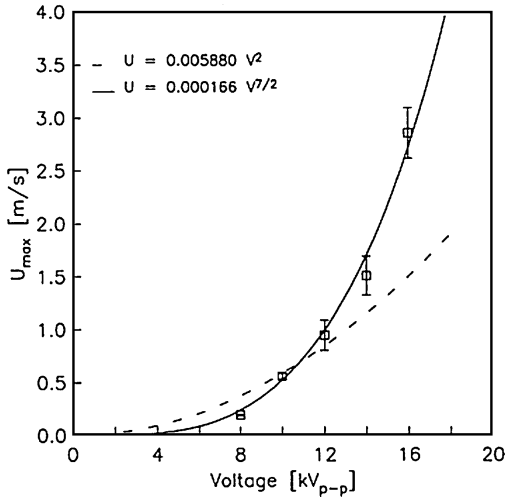

Figure 2.6: Maximum induced velocity U_{max} as peak to peak voltage V_{p-p} increases; interpolation curves and measured data points (taken from [17]).

Studies stated that even in the part of the cycle in which there is the reverse of the flow direction, the velocity component parallel to the wall never goes negative but only reduces its magnitude, meaning that the actuator actually works always in a "push-push" mode even if a "push-pull" force could be expected [14], [26]. The maximum velocity induced by the plasma actuator is proportional to the voltage as $V_{AC}^{3.5}$, as shown in Fig.2.6, and also the electrical power dissipated by the actuator and the thrust generated [14], [17]. The efficiency, as defined by Eq.2.2, appears to be controlled by the interaction at the end of the exposed electrode where the plasma generation is higher [17].

There are two types of actuation mode depending on the timescale of the actuation pulse [26], [35], [24], [43]:

- **Microsecond discharge**: pulses with durations in the order of microseconds, for which the control effect on the flow is due to the electrohydrodynamic (EHD) interaction only and the plasma can be considered almost in thermal equilibrium with the surrounding fluid [14]; maximum induced velocities are lower than 10 m/s, typically 5 to 6 m/s. In quiescent air, the actuation generates first a starting vortex and then downstream of the exposed electrode a jet is formed parallel to the wall [30].

- **Nanosecond discharge**: pulses on the order of nanoseconds inject an high amount of energy with a fast discharge that heats up the gas and generates shock waves; indeed the control is based not on the EHD force but on the propagating shock and the control authority is effective even at external flow velocities as high as 100 m/s [39], [44]. This type of actuation, on the contrary with respect to the microsecond discharge, develops a jet perpendicular to the dielectric [30].

In both cases, for the two halves of each AC cycle, the discharge mechanism is slightly different [39], [35].

2.1.2.4 DBD actuator's parameters optimization

Considering a standard DBD actuator, it is possible to improve its effectiveness by obtaining a compromise between materials limits, geometric limits and actuation limits. General practical rules are presented for each of the main parameters selected which are:

- **Electrical signal**: the input voltage for a DBD actuator is always AC and the signal is modulated both in frequency and wave shape to obtain different effects. Moreover, as mentioned before, the pulse duration is distinguished in microsecond and nanosecond.
  - **AC frequency**: there is an optimum AC frequency f_{AC} to maximize thrust but depends also on the dielectric capacitance that is proportional to the ratio ϵ/b, where ϵ is the dielectric coefficient and b is the dielectric thickness. At fixed dissipated power $W_E = VI$, if the current I increases the thrust decreases and the number of bright filaments in the plasma increases.

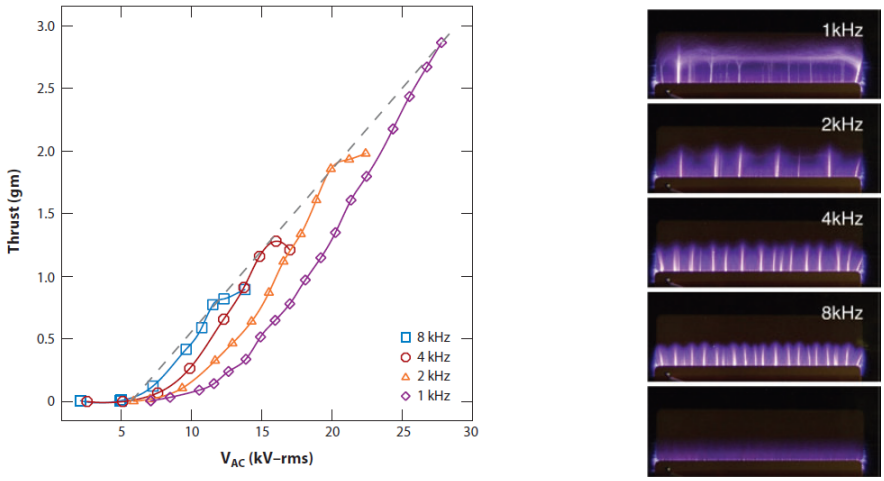

(a) (b)

Figure 2.7: Thrust generated as voltage increases for different AC frequncies (a). Plasma discharges for the different AC frequencies (b); the bottom photo shows a pure glow discharge while at the other frequencies filamentary patterns are clearly visible (taken from [14]).

The voltage at which this phenomenon occurs first is varying linearly with f_{AC} since depends directly on the power loss through the dielectric that is proportional to $f_{AC}\epsilon/b$ [14]. Fig.2.7 shows indeed this behavior.

  - **AC wave shape**: also in this case there is an optimum, and the signal distortion must be taken into account when applying to the actuator. The performances can be enhanced by increasing the duration of the duty cycle with a polarity of the pulse in which electrons are emitted by the exposed electrode, in this way more charges are deposited on the dielectric and the direct "push" mode is increased. As it is shown in Fig.2.8 the

saw-tooth indeed offers the best results. Furthermore, as general result it has been proven that the pulsed actuation consumes less power [19].

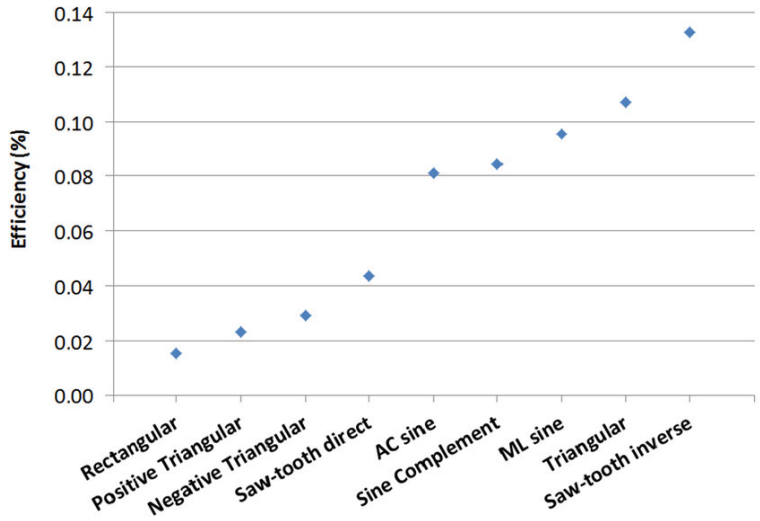

Figure 2.8: Actuator efficiency with different wave shapes (taken from [35]).

- **Dielectric**: it is at the base of the DBD actuator and its material and geometry strongly affect the behaviour of the actuator. Two characteristics must be taken into account when designing the dielectric [14]: the breakdown voltage per thickness sets the limit to the input voltage that can be safely used before the breaking of the dielectric, and the dielectric coefficient ϵ that limits the capacitance; these two depend both on the material selected and on the geometry of the insulating layer.

  - **Material**: common materials for dielectric are [24], [15]: Kapton [38], [17], polyimide and Teflon [15] for their light weight, thermal stability and dielectric strength, then other materials are glass [15] and lead tin that are heavier but grant longer durability. Plexiglass has been also used [15] with characteristics comparable to the one of Teflon. Mylar can be inserted within layers of Kapton [22], [8] to improve the total capacitance of the dielectric. In any case Kapton is the most widely used, even if expensive.
  - **Geometry**: since power losses in the dielectric are proportional to $f_{AC}\epsilon/b$, it is better to reduce the capacitance by reducing ϵ and increasing the dielectric thickness b and at the same time this improves the breakdown voltage of the insulating layer. Typically the minimum Kapton thickness to avoid breakdown is of the order of 0.05 mm, this is particularly favourable because it allows to implement thin actuators which offer minimal interference to the flow. Instead, the width of the encapsulated electrode limits the length of the plasma only if the the applied voltage is enough to establish an electric field that allows a further extension of the plasma otherwise, a further elongation of the encapsulated electrode will not extend the plasma since the electric field is not enough strong

to sustain the plasma up to the end of the electrode [17]. Regarding the thickness, it must be highlighted that increasing it, improves the dielectric resistance and increases the voltage input allowed but, a smaller thickness provides higher induced flow velocities at the same voltage; a way to combine the two qualities is the so called stair-shaped dielectric [38], [24] illustrated in Fig.2.9.

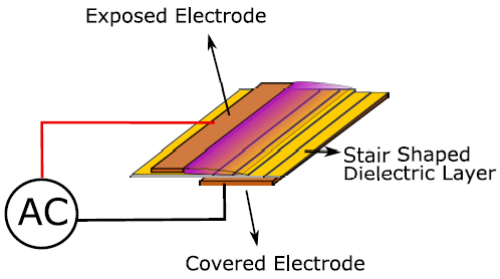

Figure 2.9: Stair-shaped actuator architecture (taken from [38]).

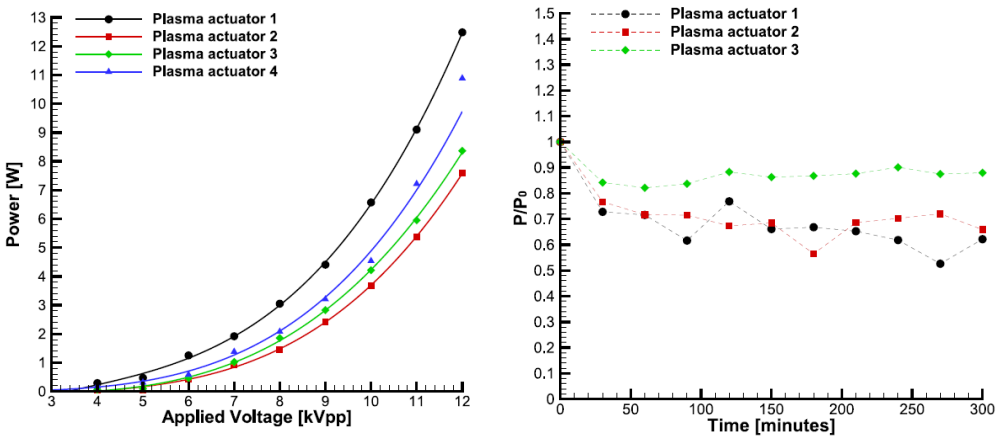

(a) (b)

Figure 2.10: Stair-shaped plasma actuator (PA) power for different inclinations of the dieletric ramp, $PA1 = 0°$, $PA2 = 3°$, $PA3 = 7°$, $PA4 = 10°$ (taken from [38]).

The important parameter in the design of a stair-shaped dielectric is the angle of inclination that layers forms at the end and indeed an optimum exists as shown in Fig.2.10. Moreover the power consumption and the operative stability are higher with respect to the standard dielectric and the plasma extends further. The last geometrical parameter is the gap distance between the two electrodes g_e, that is defined positive if there is no overlap. Said w_{ce} the width of the covered electrode, it has been found [14] that until $0 \leq g_e/w_{ce} \leq 2$ the effect on the maximum induced velocities is small whereas if the gap or the overlap is out of this range the performance decreases rapidly as the gap increases.

- **Electrodes**: common material is copper. Regarding the covered electrode,

essentially the electrode's width and the gap distance from the upper electrode, define its geometry constraints and have been already discussed at the previous point. Instead, for the exposed electrode, the most important variable is the thickness, and indeed thrust increases as thickness decreases [17].

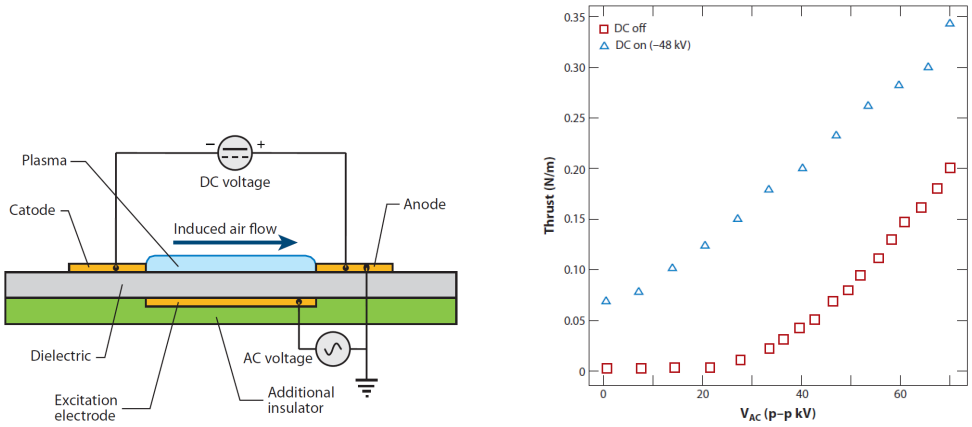

(a) (b)

Figure 2.11: DBD sliding discharge architecture (a); the thrust generated with and without DC voltage (b) (taken from[14]).

It has been developed another architecture of DBD that involves the addition of a third electrode powered with a high voltage DC signal [42], [2], [14], [35], [24]. The AC DBD is used to weakly ionize the gas while the DC potential is used to establish a corona discharge between the first and last electrode as it is shown in Fig.2.11a. The length of the discharge is bigger and the resistance to the transition from glow to arc regime is increased. Moreover, the thrust induced is noticeably increased in the sliding mode compared to the standard DBD actuator and it is present even at low V_{AC} voltage, as it is shown in Fig.2.11b. Indeed at zero AC voltage the actuator is working as pure corona discharge one.

2.1.3 Flow control applications

When dealing with flow control applications, plasma actuators are used for controlling the boundary layer and among the three types presented before the most common one is the DBD actuator. Applications are wide and different [2], up to now plasma actuators have been used for: turbulence reduction, flow separation mitigation, as vortex generator, noise reduction, heat dissipation control and aerodynamic controls. A single array aligned in cross-flow direction operated in pulsed mode proved to reduce the Tollmien-Schlichting waves instability by accelerating the fluid both downwards and along the wall-parallel direction; if the timing of the actuation is equal to the frequency of TS wave formation the effect is to attenuate even more the instability [19]. Moreover the pulsed mode with a proper duty cycle reduces dramatically the power consumption to only 12% of the continuous mode operation. For noise reduction instead the continuous mode (duty cycle of 100%) proved to be more effective on a wider range of frequencies than the pulsed mode [19], since instead of introducing perturbations timed with the instabilities, the continuous mode modifies the boundary layer velocity profile [46], [19]. The possibility of reducing flow instabilities allows to postpone the beginning of the transition from laminar to turbulent boundary layer [43], [35] and reducing the drag of 1.9% [43]. On the other side, plasma actuators can be used to generate disturbances that promotes instabilities or as vortex generators [2], [35], [43]. These approaches proved to be effective in mitigating flow separation for example of airfoils at high angle of attack. Plasma vortex generators are usually arrays of actuators aligned along the streamwise direction which induce the vortices by introducing a spanwise flow [35], [23] . If pairs of opposite of actuators are placed to form an array parallel to the flow direction, it has been noticed that persistent counter rotating vortices are generated since the opposite pairs induce jets perpendicular to the wall; this architecture, thanks to the streamwise vortices, allows to reduce drag and also heat flux from the wall [9]. Studies were done also to develop arrays of actuators aligned along the streamwise direction with both same cross flow direction [42], in such a way that by actuating in sequence a travelling wave is generated along the spanwise direction with quasi-streamwise vortices that promotes boundary layer mixing and the effect of this travelling wave is similar to the one counter rotating vortices. Other geometries that are based on non-straight electrode actuators have been investigated such as serrated [22], square, triangular and serpentine electrodes [42] and respect to the linear one, thanks to the multiple directions of the induced flow more vorticity can be generated and this improve mixing in the boundary layer.

Vortex shedding can be effectively controlled via plasma actuators both for bluff bodies and streamlined bodies [42], [24]. When evaluating the lift improvement due to multiple actuators applied on a NACA0015 airfoil, a fundamental relation has been observed such that the Strouhal number defined as $St = f_{opt}\delta/U$ is almost constant as the speed of the flow U changes [8]; f_{opt} is an optimal frequency of actuation and δ the boundary layer thickness that are both function of U. In this case the multiple arrays were put parallel to the spanwise direction and operated as opposite pairs and other combinations; lift increments up to 15% have been reported that are comparable to other case studies [2], [42], [43]. Regarding bluff bodies, vortex shedding is directly related to noise and drag, plasma actuators proved to

reduce the turbulent kinetic energy in the wake by shortening the separation region and minimizing or eliminating the vortex shedding for example on a cylinder [43]; the reduction in drag reached 50%, but must be underlined that the vortex shedding suppression is strongly related to the Reynolds number and the actuation must be adapted according to it.

Airfoils flow separation researches have shown that different types of arrays geometries are capable of improving both the pre-stall and post-stall behaviour by increasing the stall angle [23], [43], [2], [24]. While higher frequencies actuation seems to interact better with turbulence, for flow separation control lower frequencies achieve remarkable results in delaying stall. It must be underlined that typically these results refers to lower Reynolds number (typically $Re < 70000$) than standard operative conditions of aircrafts, but these actuators can be a valid solution for unmanned air vehicles, where they can be also used as aerodynamic controls improving the overall efficiency [23].

If microsecond discharge actuators are limited to low speed flows since authority decreases as external flow speed increases, nanosecond discharge actuators can be effective up to Mach number $M \approx 0.85$ [44] while spark-jet actuators are capable of granting control even at supersonic flows [43].

2.2 Wall bounded flows

Wall bounded flows collect all the flow cases in which it is present at least one solid boundary. Considering this definition, it is easy to understand the importance of studying the characteristics of these flows. Examples of wall bounded flows are internal flows such as flow through ducts and pipes but there are also external flow cases as boundary layers developing over the surface of vehicles, and even atmospheric boundary layer.

The interesting aspect of these flows, is that the mean velocity field in the region close to the solid boundaries presents a similar behaviour for all these cases.

This universal behaviour is widely exploited to carry out experiments in wind tunnels; indeed, the results obtained, can be extended then to similar conditions. As it will be explained later, the same principle is followed for the design of the test bench for the plasma actuator; in particular the flow case chosen is the fully developed channel flow that will be illustrated in the following section.

2.2.1 Fully developed channel flow

Taking into consideration the sketch in Fig.2.12 where L is the duct length, w the width and δ the half height of the channel, the geometrical characteristics of this flow can be summarized as follows [36]:

- $L/\delta \gg 1$;
- large aspect ratio of the cross section so, $w/\delta \gg 1$.

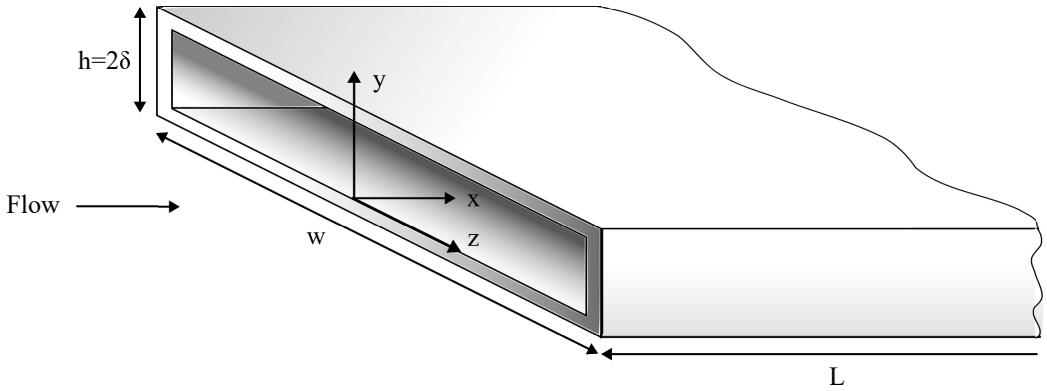

Figure 2.12: Sketch of a channel flow (origin of axes fixed at the channel inlet).

The first condition grants that there is enough space for the flow to evolve and be statistically independent of x, so the region of interest is actually not the entire duct but from the point at which the flow can be reasonably stated to be fully developed. The large aspect ratio set by the second requirements instead, is necessary to minimize the influence of the side walls thus establishing a theoretical 2D condition that yields the independence of the flow statistics from the z-axis. Moreover, thanks to the symmetry of the geometry the statistics at $z > 0$ and $z < 0$ are equal and the same can be said for $0 < y < \delta$ and $\delta < y < 2\delta$. Hence in the fully

developed region the flow could be considered statistically stationary and statistically one-dimensional since only dependency on y is left.

Assuming the 2D fully developed incompressible conditions stated before, now it will be derived the set of equations for the mean flow.

Set $\mathbf{U}(\mathbf{x},t) = (U,V,W) = (U_1,U_2,U_3)$ the velocity field with $\mathbf{x}$ the position, t the time, and U,V and W its components along x, y, and z axis respectively (as sketched in Fig.2.12), the Reynolds decomposition reads as following:

$$\mathbf{U}(\mathbf{x},t) = \langle \mathbf{U}(\mathbf{x},t) \rangle + \mathbf{u}(\mathbf{x},t). \tag{2.4}$$

so, the velocity field is recasted as the sum of its mean field $\langle \mathbf{U}(\mathbf{x},t) \rangle$ and fluctuating part $\mathbf{u}(\mathbf{x},t)$. By applying Eq.(2.4) into the continuity equation and applying the averaging operation it results that:

$$\nabla \cdot \langle \mathbf{U} \rangle = 0. \tag{2.5}$$

for ease of notation, the dependence on position and time of all fields will be omitted. Eq.(2.5) states that the mean velocity field is solenoidal too. Moving on to the momentum equations, after applying the mean, substituting Eq.(2.4) and recalling Eq.(2.5), the Navier-Stokes equations transform into:

$$\frac{\partial \langle U_j \rangle}{\partial t} + \langle U_i \rangle \frac{\partial \langle U_j \rangle}{\partial x_i} = \frac{\partial}{\partial x_i} \left[\nu \left(\frac{\partial \langle U_i \rangle}{\partial x_j} + \frac{\partial \langle U_j \rangle}{\partial x_i} \right) - \frac{1}{\rho} \langle p \rangle \delta_{ij} - \langle u_i u_j \rangle \right]. \tag{2.6}$$

the so called Reynolds equations. If now are applied the aforementioned conditions satisfied by the 2D fully developed channel flow this set of equations dramatically simplifies and useful relations will be derived. Beginning from the mean continuity equation it reduces to:

$$\frac{d\langle V \rangle}{dy} = 0. \tag{2.7}$$

Since 2D assumption implies $\langle W \rangle = 0$, whereas $\langle U \rangle$ is independent of x and $\langle V \rangle$ depends only on y, integrating Eq.(2.7) with boundary conditions $\langle V \rangle_{y=0} = \langle V \rangle_{y=2\delta} = 0$ results in $\langle V \rangle = 0$ for all y. Considering this result the mean momentum balance along y simplifies as:

$$0 = -\frac{d}{dy} \langle v^2 \rangle - \frac{1}{\rho} \frac{\partial \langle p \rangle}{\partial y}. \tag{2.8}$$

which, with the boundary conditions $\langle v^2 \rangle_{y=0} = \langle v^2 \rangle_{y=2\delta} = 0$ integrates to:

$$\langle v^2 \rangle + \frac{\langle p \rangle}{\rho} = \frac{p_w(x)}{\rho}. \tag{2.9}$$

where $p_w(x) = \langle p(x,0,0) \rangle$ is the mean pressure on the bottom wall (symmetrically equal to the one on the top wall). Moreover, differentiating Eq.(2.9) with respect to x, the following relation is found:

$$\frac{\partial \langle p \rangle}{\partial x} = \frac{dp_w}{dx}. \tag{2.10}$$

which means that the axial gradient of the mean pressure is constant across the flow. Regarding the mean momentum along x instead:

$$0 = \nu \frac{d^2\langle U \rangle}{dy^2} - \frac{d}{dy}\langle uv \rangle - \frac{1}{\rho}\frac{\partial \langle p \rangle}{\partial x}. \tag{2.11}$$

and defined the total shear stress $\tau(y)$:

$$\tau(y) = \nu\rho \frac{d\langle U \rangle}{dy} - \rho\langle uv \rangle. \tag{2.12}$$

by substituting Eq.(2.10) and Eq.(2.12) in Eq.(2.11) the following relation can be derived:

$$\frac{d\tau}{dy} = \frac{dp_w}{dx}. \tag{2.13}$$

This states that the cross-stream shear-stress gradient is balanced by the axial normal stress gradient. Moreover, since τ is a function only of y and p_w only of x from Eq.(2.13) can be inferred that both dp_w/dx and $d\tau/dy$ are constant. Then, since $\tau(y)$ is antisymmetric with respect to the mid-plane of the channel ($y = \delta$), there is $\tau(\delta) = 0$, $\tau(2\delta) = -\tau(0) = \tau_w$. Hence the solution to Eq.(2.13) is:

$$\frac{dp_w}{dx} = -\frac{\tau_w}{\delta}. \tag{2.14}$$

and:

$$\tau(y) = \tau_w \left(1 - \frac{y}{\delta}\right). \tag{2.15}$$

This is an important deduction since implies that for a given pressure gradient dp_w/dx and channel half-height δ, the total shear-stress profile is linear and independent on flow regime (whether laminar or turbulent) and fluid properties (density ρ and viscosity ν).

To characterize the channel flow, two Reynolds number can defined:

$$Re = \frac{2\delta\bar{U}}{\nu}. \tag{2.16}$$

$$Re_0 = \frac{\delta U_0}{\nu}. \tag{2.17}$$

where $U_0 = \langle U \rangle_{y=\delta}$ is the average U at the centerline, and $\bar{U}$ is the so called bulk velocity:

$$\bar{U} = \frac{1}{\delta}\int_0^\delta \langle U \rangle dy. \tag{2.18}$$

and for this reason Re defined as Eq.(2.16) is referred to as bulk Reynolds number. Actually a third Reynolds number can be used, the so called friction Reynolds number. Considering the total shear stress $\tau(y)$, Eq.(2.12) highlights two contributions: the viscous term $\nu\rho d\langle U \rangle/dy$ and the Reynolds stress $-\rho\langle uv \rangle$. The boundary conditions set $\mathbf{U} = 0$ so the Reynolds stress is zero at the wall whereas the viscous contribution is equal to τ_w.

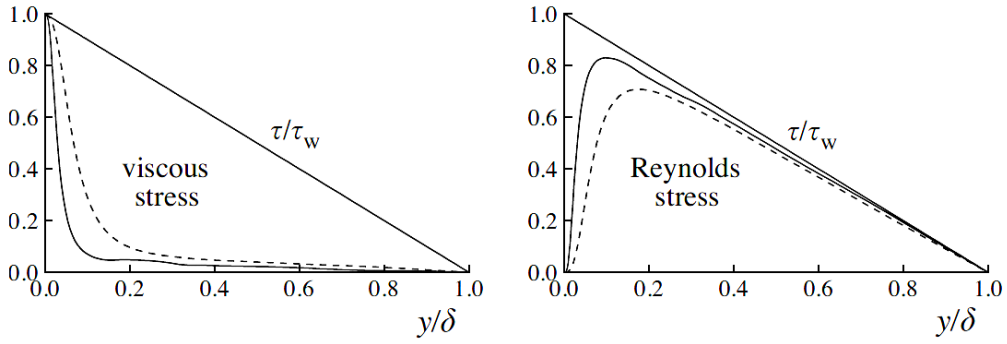

Figure 2.13: Profiles of viscous and Reynolds shear stress in turbulent channel flow: dashed line $Re = 5600$, solid line $Re = 13750$ (taken from [36]).

Focusing on Fig.2.13, it is evident that in the near wall region where y/δ becomes small, the main contribution to τ is due to the viscous term and so ν and τ_w become important parameters. Following this concept, viscous scales are introduced which are appropriate velocity and lengthscales in the near wall region. They are, the friction velocity:

$$u_\tau = \sqrt{\frac{\tau_w}{\rho}}. \tag{2.19}$$

and the viscous lengthscale:

$$\delta_\nu = \nu\sqrt{\frac{\rho}{\tau_w}} = \frac{\nu}{u_\tau}. \tag{2.20}$$

from these quantities then, it could be derived the friction Reynolds number aforementioned:

$$Re_\tau = \frac{u_\tau \delta}{\nu} = \frac{\delta}{\delta_\nu}. \tag{2.21}$$

and distance y from the wall can be recasted as fraction of wall units giving the non-dimensional parameter:

$$y^+ = \frac{y}{\delta_\nu}. \tag{2.22}$$

Taking into account this definition, the near wall region can be divided into several layers depending on the importance of the two contributions, the Reynolds stress and the viscous term, to the the total shear stress τ. First of all, two big layers can be identified: the inner layer where $y/\delta < 0.1$ in which $\langle U \rangle$ is determined by viscous scales u_τ and y^+ independently of U_0 and δ, and the outer layer for $y^+ > 50$ where direct effects of viscosity on $\langle U \rangle$ are negligible. Then, these layers can be further divided as presented in Tab.2.1.

Recalling now the gradient of the mean axial velocity, it can be recasted as:

$$\frac{d\langle U \rangle}{dy} = \frac{u_\tau}{y}\Phi\left(\frac{y}{\delta_\nu}, \frac{y}{\delta}\right). \tag{2.23}$$

Table 2.1: Near-wall regions and properties (according to definitions of [36]).

Regions	**Range**	**Properties**
Viscous sublayer	$y^+ < 5$	The Reynolds stress is negligible with respect to the viscous stress.
Buffer layer	$5 < y^+ < 30$	The magnitude of the Reynolds stress is comparable to the viscous stress. It is the region of transition between the viscous-dominated and turbulence-dominated parts of the flow.
Overlap region	$y^+ > 50$, $y/\delta < 0.1$	Region of overlap between inner and outer layer (at high Re).

where Φ is a non-dimensional function. In this way, the dependence on y is scaled with a inner lenghtscale, δ_ν, and also outer lengthscale δ. Since in the inner layer it is assumed that the mean velocity profile is independent of δ and U_0, Φ will be function only of $y/\delta_\nu = y^+$ and defined:

$$u^+ = \frac{\langle U \rangle}{u_\tau}. \tag{2.24}$$

the so called law of the wall reads as:

$$u^+ = f_w(y^+) = \int_0^{y^+} \frac{1}{y'} \Phi(y') dy'. \tag{2.25}$$

In the viscous sublayer, assuming y^+ small and applying the no-slip condition $f_w(0) = 0$ which implies $f'_w(0) = 1$, the Taylor expansion for $f_w(y^+)$ reduces to:

$$u^+ = y^+ + \mathcal{O}(y^{+2}). \tag{2.26}$$

So, the u^+ profile in the viscous sublayer can be assumed with good approximation to be linear. Moving to higher y^+ the effect of viscosity decreases and from $y^+ > 30$ to the end of the inner layer also the dependence on y^+ can be neglected and Φ becomes a constant equal to $1/k$ and the mean velocity gradient will be:

$$\frac{du^+}{dy^+} = \frac{1}{y^+ k}. \tag{2.27}$$

which integrates to:

$$u^+ = \frac{1}{k} \ln y^+ + B. \tag{2.28}$$

This is the so called log law. B and k are constants and in literature there is some variation in the values (as well as in the definition of the layers' ranges) and indicatively in [36] are reported $k = 0.41$ and $B = 5.2$. The log law defines another region, the log law region in which the agreement between this relation and the data at different high Reynolds number confirms Eq.(2.28). This region approximately extends from $y^+ \approx 30$ to $y/\delta \approx 0.3$. Fig.2.14 shows indeed this behaviour which is confirmed both experimentally and with DNS simulations.

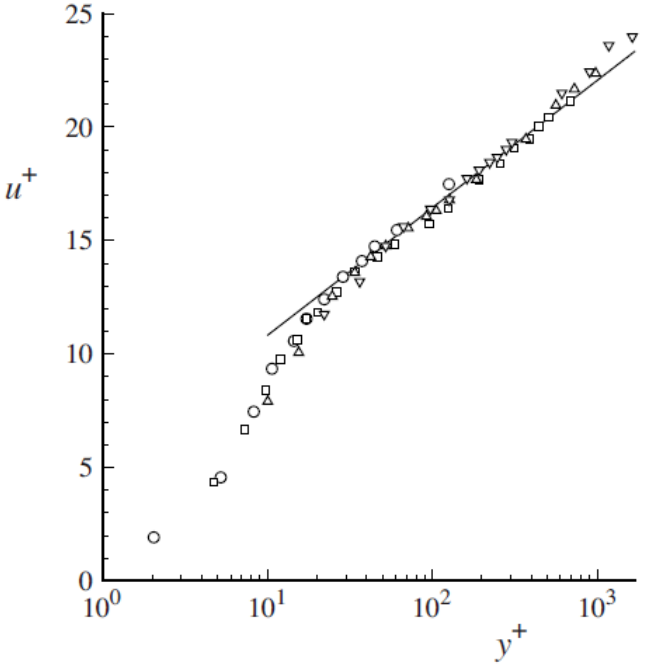

Figure 2.14: Mean velocity profile, in inner units, measured by Wei and Willmarth (1989): ◯ $Re_0 = 2970$, □ $Re_0 = 14914$, Δ $Re_0 = 22776$, ∇ $Re_0 = 39582$ and the line is the log law Eq.(2.28) (taken from [36]).

In the outer layer instead Φ tends asymptotically to a function only of y/δ. Differently from the inner layer, in this case it is defined the velocity defect law as:

$$\frac{U_0 - \langle U \rangle}{u_\tau} = F_D\left(\frac{y}{\delta}\right) = \int_{y/\delta}^{1} \frac{1}{y'}\Phi(y')dy'. \tag{2.29}$$

unlike the law of the wall, there is no suggestion that the velocity defects law is universal so depends on the actual flow. Said Φ_I the relation Φ simplified for the inner layer and Φ_O for the outer layer, at sufficiently high Reynolds number ($Re > 20000$) an overlap region between the inner and outlayer exists and there both Φ_I and Φ_O holds. This means that:

$$\frac{y}{u_\tau}\frac{d\langle U \rangle}{dy} = \Phi_I(y^+) = \Phi_O(\frac{y}{\delta}) = \frac{1}{k}. \tag{2.30}$$

this leads to a relation similar to the log law also for velocity defect law for $y/\delta \ll 1$:

$$F_D\left(\frac{y}{\delta}\right) = -\frac{1}{k}\ln\left(\frac{y}{\delta}\right) + B_1. \tag{2.31}$$

where B_1 is a constant depending on the flow.

Chapter 3

Test bench design

In order to fully characterize the behaviour of a plasma actuator both electrical and flow control properties must be analysed, possibly at the same time, to directly correlate different data. This allows a more comprehensive understanding of the complex physical processes involved and the performances of the actuator. As will be explained in the following sections, measuring accurately data about the flow interacting with the actuator, presents challenging problems in terms of safety (high voltages, production of ozone) and reliability of the acquired information (strong near-wall gradients, electrical interference with measurements equipments). Considering all this aspects, it has been proposed the following set-up. A 2D turbulent fully-developed channel flow has been chosen for these reasons:

- The flow is a benchmark widely studied both numerically and experimentally, so a large amount of data is available for comparisons;
- One of the main goal of most of the recent plasma actuators developed world-wide is drag reduction in turbulent flows; skin friction, which is the main contribution to drag in this case, depends on near-wall velocity field, that has universal behaviour, so the results obtained during experiment in this facility can be extended to other cases;
- The channel flow is designed to have a cross-section geometry to replicate at best the bidimensional approximation, the influence of side walls is minimized offering conditions similar to real vehicles aerodynamics applications;
- The actuator acts in a flow that can be easily controlled and on which external disturbances have a minimal influence, granting more stable measurements;
- The actuator is inside the tunnel so, it is safer during operations.

For the flow measurements, planar PIV (Particle Image Velocimetry) technique has been judged to be the best proposal since:

- The interest of this work is the velocity field and the available techniques are [26]:
  - HWA (Hot Wire Anemometry): it offers good time-resolved near-wall point measurements but cannot be used in presence of plasma because

both the actuator and the probe highly interfere electrically each other and, temperature gradients due to plasma generation increases measurements uncertainties. So, the HWA can be only safely used at enough distance from the actuator;

  - Pitot tube: specific probes made of insulating materials can be used close enough to the plasma source even if also this sensor can interfere with the actuator due to charge accumulation on the probe. The measurement also in this case is time resolved and local, and due to probe-wall interference is not capable of reaching near-wall information;
  - PIV (Particle Image Velocimetry): considering only the planar case, the vector field obtained depicts simultaneously more details about the flow than the previous techniques with minimal interference with the flow. Nevertheless, also this approach is not completely free from problem related to ionization, indeed the seeding used for flow visualization can be ionized too and react to the strong electromagnetic field;
  - LDV (Laser Doppler Velocimetry): can be a compromise between HWA and PIV but even if has the advantages of greater time resolution with respect to PIV and is less intrusive with respect to HWA still suffers of the same seeding problems of PIV and it is a local measure as HWA.

- For performance analysis the limitations on time resolving capabilities of standard PIV is not an issue since the transient is not of importance itself and time averaged quantities are considered for the computation of efficiency as defined in equation 2.2. So the rich spatial information that a PIV can give is more important than the time resolution that other techniques offer. Moreover, it can be used to extrapolate the thrust produced by the actuator [28].

Regarding electrical quantities, the electrical power will be computed with a common technique based on the Lissajous curves.

The 2D fully developed channel flow will be realised by designing a specific wind tunnel. Each part of the test bench, i.e. wind tunnel, PIV measurements set-up and electrical measurements will be presented in the following section together with the theoretical background.

3.1 Wind tunnel

Designing a wind tunnel means trying to replicate all the relevant features of a flow. Depending on the case, the flow itself can be the subject of the experiment or the interactions between the flow and an object inside [7], [10]. Basically, the wind tunnel allows to scale the real flow case in order to perform tests and analysis in a more controlled environment and obtain results that could be extended to several cases with comparable characteristics. This is the practical application of the similarity principles. The aforementioned generality of the results obtained with experiments is the direct consequence of proper adimensionalization of the physical variables involved. Thanks to Buckingham theorem the number of independent parameters that required to characterize a phenomenon can be reduced and these non-dimensional parameters found, can be used to verify similarity within apparently different conditions. Moreover, reducing the number of parameters has another simple benefits on the experiments: less parameters implies less test required. However, the Buckingham theorem even if is based on physical homogeneity of variables, is a purely mathematical operation and thus requires a previous physical understanding of the equations and variables involved since also the non-dimensionalization is not unique [16].

Among all the non-dimensional parameters, for wind tunnel experiments three are the most relevant [7], [16].Said ρ the fluid density, L a typical lengthscale, V a typical velocity scale, μ the fluid dynamic viscosity and a the speed of sound of the fluid, these parameters are:

- Reynolds number:

$$Re = \frac{inertia forces}{viscous forces} = \frac{\rho L^2 V^2}{\mu V L} = \frac{\rho L V}{\mu}$$

- Mach number:

$$M = \sqrt{\frac{inertia forces}{elastic forces}} = \sqrt{\frac{\rho L^2 V^2}{\rho a^2 L^2}} = \frac{V}{a}$$

- Froude number (defined considering as external force only gravity [7]):

$$Fr = \sqrt{\frac{inertia forces}{gravitational force}} = \sqrt{\frac{\rho L^2 V^2}{\rho g L^3}} = \frac{V}{\sqrt{gL}}$$

If these parameter are the same both for the actual and scaled condition, the two systems are dynamically similar. Usually, except the cases in which are present unsteady boundary conditions or volume forces such as gravity or dynamic tests with towed bodies, the Froude number can be neglected. Indeed, Froude number is a parameter typically considered for tests in facilities where an interface between two fluids is presents and the body interacts with this boundary (for example water tunnel for ships). From now on the discussion will be focused only on air tunnel.

Depending on the Mach number it can be be distinguished these types of wind tunnels [16]:

- **Low-speed subsonic** wind tunnels: with $M < 0.3$;
- **High-speed subsonic** and **transonic** wind tunnels: compressibility effects are present and $M < 1.3$;
- **Supersonic** wind tunnels: $M \leq 4$ but can reach even $M \leq 5$;
- **Hypersonic** wind tunnels: $M > 5$.

As Mach number increases the complexity of the facilities increases as well as heat and dissipation problems. As consequence the power demand for driving the flow raises with the order of V^3. But, the flow regime is characterized by the Reynolds number too, that has a primary role in subsonic wind tunnels and gives qualitative information about the state of the flow, whether it is turbulent or laminar.

When talking about Re and M of a flow regime of course must be specified that they are referred to the test section of the wind tunnel and this affects the geometry of the facility. Indeed the design of a wind tunnel starts from its test section. The steps of the process can be different but usually firstly a range of (Re,M) is chosen and represent the flow regimes which are of interest for the investigations. Disregarding the categories of supersonic and hypersonic wind tunnel which require much different plants compared to transonic and subsonic facilities [16], it can be identified two types of tunnels, open and closed loop [16], [7], [10]:

- **Open-loop**: the fluid driven in the circuit is continuously flowing inside and outside from the surrounding environment; in Fig.3.1 are shown two possible configurations;
  - Advantages:
    i. usually cheaper compared to closed loop;
    ii. widely used for fundamental flow phenomena investigations, there is no accumulation of seeding particles used for flow visualization and optical techniques;
    iii. no accumulation of exhausts produced by chemical reactions.
  - Disadvantages:
    i. Higher power consumption since the flow must be continuously accelerated;
    ii. More affected by external disturbances, so flow conditioners are extremely important to damp undesired fluctuations;
- **Closed-loop**: the same volume of fluid is circulating in the circuit without exchanges with the external environment as shown in Fig.3.2;
  - Advantages:
    i. Higher flow quality in the test section and less affected by external disturbances;
    ii. Lower operational costs since once the flow is circulating in the tunnel the driving system must overcome only the pressure losses;
  - Disadvantages:

i. The structure of the tunnel is more complex and corners must be carefully designed to avoid separation; moreover the heat dissipation is important to avoid undesired temperature increment;

ii. Problems when using seeding for flow visualization can raise due to excessive accumulation of tracer particle; the same could happen for exhausts produced by chemical reactions and so a purge system should be installed in the plant.

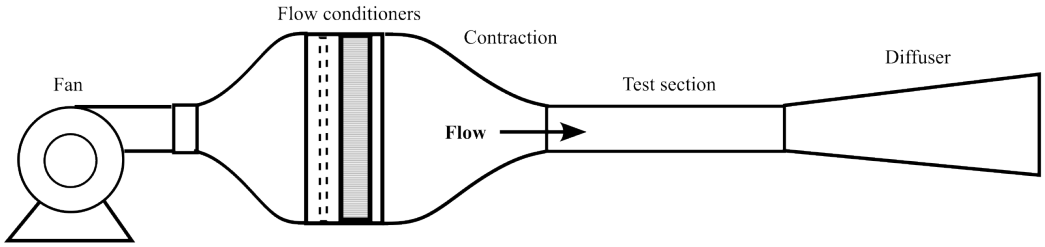

(a) Blower type.

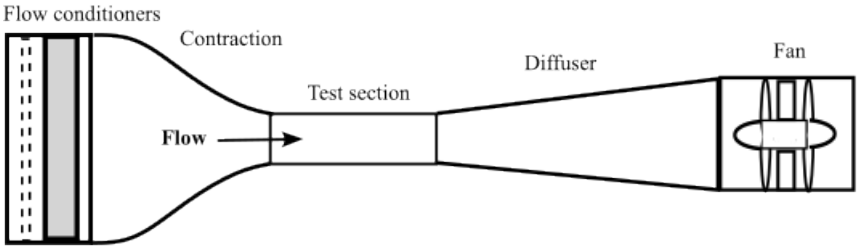

(b) Suction type.

Figure 3.1: Open-loop wind tunnel configurations.

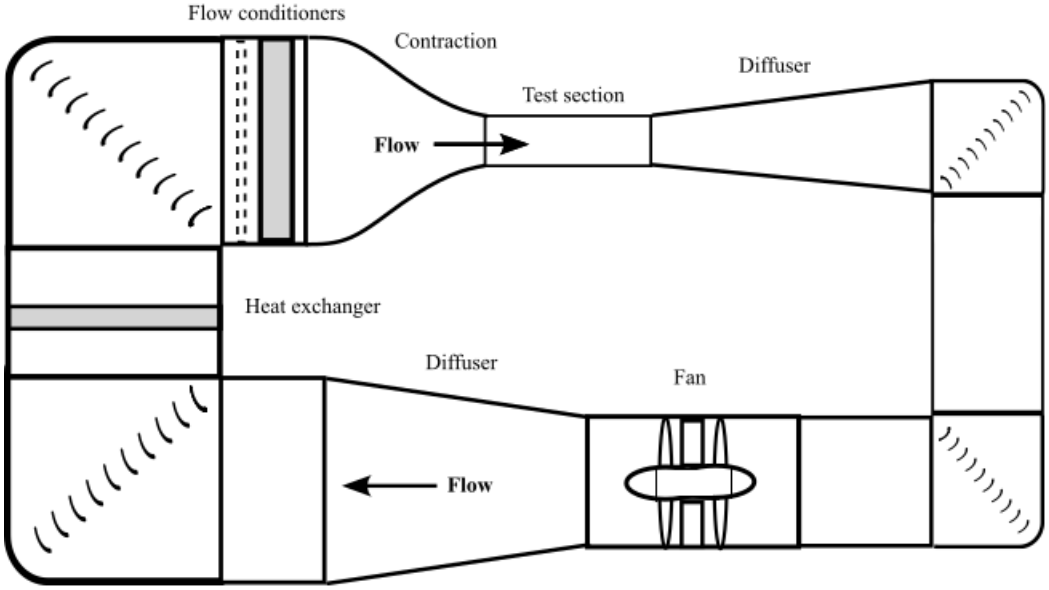

Figure 3.2: Closed-loop wind tunnel configuration.

Since the 1930s, researchers where focused on reducing the effects of disturbances that could deteriorate the flow quality and increase the turbulence level. Early suction wind tunnels were particularly affected by these problems and moreover, due to the particular geometry the pressure in the test section is lower than ambient pressure thus requiring a proper sealing of any aperture; the main advantage of this configuration is the position of the fan at the exit that reduces the influence of disturbances due to the rotating fan. Blower type instead, could reach higher performances and the drawbacks of having a lower pressure in the test section can be simply eliminated by removing the final diffuser [34]. Indeed the diffuser is placed mainly for improving the pressure recovery and reducing power losses so, if the requirements on the test section are more important it can be omitted [33]. In general, for small size subsonic wind tunnels, the centrifugal blower is much more convenient than axial fans because [34], [33] the former one can operate at wider flow conditions granting reasonable steadiness and efficiency as well as a lower noise level and pulsation even at off-design conditions. However, axial fans (sometimes even multistage plants) are the best solution when the consumptions are a primary issue, since the efficiency can be of the order of 90% if opearating conditions satisfy the design specifications [34]. For this reasons even if closed wind tunnels have in general superior performance especially in terms of required power, open loop blower type are an effective solution especially for subsonic experiments when the length of the facility is not prohibitive.

In the following sections will be presented the design implemented for the actual test bench. As type it has been chosen a subsonic blower configuration, that it has been designed to use as driving stage the already available PAT (Planar Air Tunnel) [5], [18], this affected the final dimension of the tunnel. The steps followed are:

1. **Test section requirements definition**: operating Re, cross section geometry, section length, apertures' position;

2. **Contraction design**: outlet speed, upstream and downstream cross section matching, length, shape.

Since the power requirements were a minor issue, the diffuser is omitted in favour of improved test section management and lower final length.

3.1.1 Test section

Introduced the key features of the flow case that the test section should replicate, now it will be presented the steps followed for its design.

The procedure used began with the definition of the viscous lengthscale value. Since the measurements will be done exploiting PIV technique, the image resolution sets the limit to the maximum spatial resolution available, effective pixel size is used as reference. The aim of the design is to obtain a good resolution at least up to the end of the viscous sublayer ($y+ > 5$) by combining PIV set up and channel dimensions. To achieve this results an optimization problem has been defined and implemented. The constraints on the design on the cross section are directly linked to the one of the PIV set up and they are:

- $Re > 3000$: to be turbulent and avoid transitional effects [36];

- w fixed: the maximum width is limited by the width of the PAT;
- viscous lengthscale δ_ν at least equal to twice the maximum resolution of PIV set up;

Moreover, some test cases shown in Tab.3.1 where considered as benchmark. Despite the scatter of the data, the aspect ratio of the cross-section $w/2\delta$ is always greater than 10:1 even if it is reported in [31] and [47] that the minimum value to grant two-dimensional condition is 7:1.

Table 3.1: Test cases with their relevant channel properties.

Test cases	$w/2\delta$	L/δ	Re_0	**Contraction ratio**
Laufer [29]	12:1	86	12300-61600	29:1
Comte-Bellot [13]	13.3:1	122	57000-230000	8:1
Clark [12]	12:1	120	10000-130000	10:1
Hussain [20]	18:1	450	13000-32500	3.6:1
Zanoun [47]	12:1	260	120000	(not specified)
Lien [31]	11.7:1	450	40000-185000	9:1

Actually another constraint subsists on the cross section. The PAT not only limits the maximum width w but also the the channel height h. This has a direct effect on the acceptable values of the contraction ratio CR that must match:

- Cross section geometry of the PAT outlet and the channel inlet;
- Flow speed reached at the contraction outlet that sets the Reynolds number;
- Contraction limits to have a good flow quality which in general ranges between 6 to 9 [34], [7].

An iterative procedure has been proposed to find the optimum design parameters. The steps implemented are the following:

- **Step 1**: set desired viscous lengthscale δ_ν and report PAT cross section parameters (inlet height h_i and width w that is the same for the channel);
- **Step 2**: set first guess for bulk Reynolds number Re;
- **Step 3**: compute half channel height δ as function of Re;
- **Step 4**: compute aspect ratio $w/2\delta$ and if $w/2\delta < 10$ update coefficient for reducing Re;
- **Step 5**: compute contraction $CR = h_i/2\delta$ and update coefficient for reducing Re if $CR < 6$ and increasing Re if $CR > 9$;
- **Step 6**: update Re with an increment obtained as linear combination of coefficients computed at Step 4 and 5 each moltiplied for a coefficient that scales its value depending on the priority assigned to the condition used for that coefficient (weighted updated);

- **Step 7**: repeat steps from 3 to 6 until the updating increment is zero.

In order to compute $\delta(Re)$ at Step 3, as good approximation, the following relation [36] was implemented:

$$\delta = \delta_\nu Re_\tau \approx \delta_\nu 0.09 Re^{0.88}. \tag{3.1}$$

Then, once δ has been estimated, Re is already computed, and $Re_\tau = \delta/\delta_\nu$ and $CR = h_i/2\delta$. Moreover, another simple approximation can be used to find the centerline mean velocity U_0:

$$U_0 \approx 5u_\tau \log_{10} Re. \tag{3.2}$$

Assuming the profile independent of z-direction and symmetric with respect to channel mid-plane, the mean flow rate can be simply computed as:

$$Q = \int_0^{2\delta} \int_{-w/2}^{w/2} \langle U(y,z) \rangle dz dy = w \int_0^{2\delta} \langle U(y) \rangle dy. \tag{3.3}$$

and recalling Eq.(2.18), Eq.)(3.3) can be reduce to:

$$Q = w \int_0^{2\delta} \langle U(y) \rangle dy = w 2\delta \bar{U} = w\nu Re. \tag{3.4}$$

since the bulk velocity can be recasted as $\bar{U} = Re\nu/2\delta$.

Table 3.2: Preliminar test section parameters and results obtained with the proposed algorithm.

Input parameters	
ν	$1.6677 \cdot 10^{-5}\ m^2/s$
δ_ν	$10\ \mu m$
w	$450\ mm$
h_i	$180\ mm$
Results	
δ	$20\ mm$
Re	87003
Re_0	49395.5
Re_τ	2000
u_τ	$1.668\ m/s$
$\bar{U}$	$36.27\ m/s$
U_0	$41.18\ m/s$
$w/2\delta$	11.25
CR	4.5
Q	$0.6529\ m^3/s$

In Tab.3.2 are reported the final parameters of the cross section and the flow regime achievable with that geometry. It can be noticed that the contraction ratio CR is actually out of the aforementioned range of $6 < CR < 9$. Indeed it has been necessary to relax this constraint otherwise the problem converges to a solution with

$CR = 9$ which implies channel height of only 2 cm, too small for a good resolution at intermediate y^+ values.

Regarding the channel length, that is linked to the fully developed condition, there is no common agreement on the definition of a minimum lenght at which the flow can be termed fully developed. Indeed, as reported in [31], early works on two-dimensional channel facilities were performed with the measurements' location even at only $x/\delta = 46$ from the entrance while more recent works shifted the limit at $x/\delta > 200$. For the present case it has been chosen to set a minimum $x/\delta = 90$ to limit the size of the facility and final costs. This reduces the final channel lenght to ~ 2700 mm or $L/\delta \sim 135$. If some transition phenomena appears during tests, tripping devices will be added at the channel inlet to promote a quick transition.

3.1.2 Contraction

The contraction is a fundamental part of every wind tunnel whatever it is a blower, a suction or a closed-loop wind tunnel [7]. The effects of the cross section on the flow are [34]:

- Increase flow mean velocity: in this way, sections with flow conditioners can be placed in larger cross section, thus reducing power losses;
- Improving flow quality by reducing turbulence intensity and increasing uniformity.

Indeed considering an axisymmetric contraction and assuming inviscid flow, it is estimated that the reduction in variation of the mean velocity is for each of the three components [32]:

$$\frac{\Delta u_e}{\langle U_e \rangle} \approx \frac{1}{CR^2} \frac{\Delta u_i}{\langle U_i \rangle}. \tag{3.5}$$

$$\frac{\Delta w_e}{\langle W_e \rangle} = \frac{\Delta v_e}{\langle V_e \rangle} \approx \frac{1}{\sqrt{CR}} \frac{\Delta v_i}{\langle V_i \rangle}. \tag{3.6}$$

where Δu, Δv and Δw are the variations of the velocity for each component and subscripts "e" and "i" identify respectively exit and inlet position. It is clear that the axial component is the most affected by the contraction. Moreover, other relations can be found for the turbulence intensity along the three components of velocity:

$$\frac{u_{rms_e}}{\langle U_e \rangle} \approx \frac{1}{CR^2} \sqrt{\frac{3}{4}(\ln(4CR^3) - 1)} \frac{u_{rms_i}}{\langle U_i \rangle}. \tag{3.7}$$

$$\frac{w_{rms_e}}{\langle W_e \rangle} = \frac{v_{rms_e}}{\langle V_e \rangle} \approx \sqrt{\frac{4}{3CR}} \frac{v_{rms_i}}{\langle V_i \rangle}. \tag{3.8}$$

u_{rms}, v_{rms} and w_{rms} being the root mean squares of the turbulent fluctuations. It must be pointed that these relations constitute only a reference for the general effect of the contraction of the velocity field, indeed assuming the flow inviscid is a strong simplifying hypothesis in some cases and viscous dissipation usually is the main contribution in power losses in the contraction [21].

The design of the contraction must match the requirements on flow quality and final speed at its outlet. Several geometries have been studied in literature [4], [1], varying the contraction shape and ratio, but the most important things to care are two: the length should be enough high to reduce occurrence of flow separation but enough short to minimize boundary layer growth, friction losses and costs and the CR should be as high as possible to have good flow quality but not too big to avoid separation. It is evident that these two condition are strictly coupled and for this reason as general rule is reported that $6 < CR < 9$ [7], [32], [1], [34] as it was stated in the previous section. There exist different polynomial and non-polynomial curves used for contraction shapes; usually polynomial functions do not require to determine the coefficients through optimization of the geometry, which can be performed with potential flow simulations (panel methods) or RANS. For the present work, it has been selected the following polynomial curve of the 5^{th} order [4], which is a quite common option:

$$h(x) = h_i - (h_i - h_e)\left(6\left(\frac{x}{l_c}\right)^5 - 15\left(\frac{x}{l_c}\right)^4 + 10\left(\frac{x}{l_c}\right)^3\right). \tag{3.9}$$

where h_i and h_e are the inlet and exit height respectively and l_c is the contraction length. For this geometry [4] performed analysis at $CR = 7.7$ with a 2D contraction and stated flow separation at inlet for $l_c/h_i < 0.667$ and for $l_c/h_i > 1.79$ at the outlet due to an adverse pressure gradient established after an excessive growth of the boundary layer, that makes it susceptible to separation. Thus, $l_c/h_i = 1$ was set meaning $l_c = 180\ mm$.

The test section and the PAT constrain the geometry of the cross section that must be rectangular. For this shape, the flow near the walls tends to naturally migrate laterally and especially the boundary layer near corners is more liable to separate. Moreover, for 2D contraction as it is the case of this wind tunnel, strong secondary flows can develop from thick boundary layers of the flat walls. The interference of these secondary flows will be investigated during the characterization of the flow uniformity of the real convergent, even if can be reasonably hypothesized that the high aspect ratio of the cross section should limit the effects in the region near the side walls.

3.1.3 Power losses estimation

Once the final layout is defined, in general the driving system is selected to overcome the power required to move the fluid in the plant. In this case the PAT has already a driving system constituted by a centrifugal blower that cannot be changed. Thus the estimation of the power losses in this case is fundamental for understanding if the part added to the PAT i.e., the channel and the convergent, must be modified.

Considering inviscid, irrotational flow Bernoulli equation reads as following:

$$H = \rho g z + p_{static} + \frac{1}{2}\rho U^2 = const. \tag{3.10}$$

where g is the gravitational acceleration and z the piezometric height. Considering small tunnel height, the influence of the term $\rho g z$ can be disregarded since introduces negligible variations and so the equation can be recasted as:

$$p_{static} + \frac{1}{2}\rho U^2 = p_{total} = const. \tag{3.11}$$

But actually the hypothesis of inviscid and irrotational fluid are not in general satisfied and the total pressure p_{total} is no more constant and decreases due to concentrated and distributed losses. For example, in a straight duct main total pressure losses will be distributed and mainly due to friction while for screens the pressure drop will be concentrated. It is defined the local loss coefficient of a section, the total pressure drop in the section over the dynamic pressure at the inlet of the section:

$$K_{local} = \frac{\Delta p_{total}}{\frac{1}{2}\rho U_i^2}. \tag{3.12}$$

where subscript "i" stands for inlet position.

3.1.3.1 PAT losses

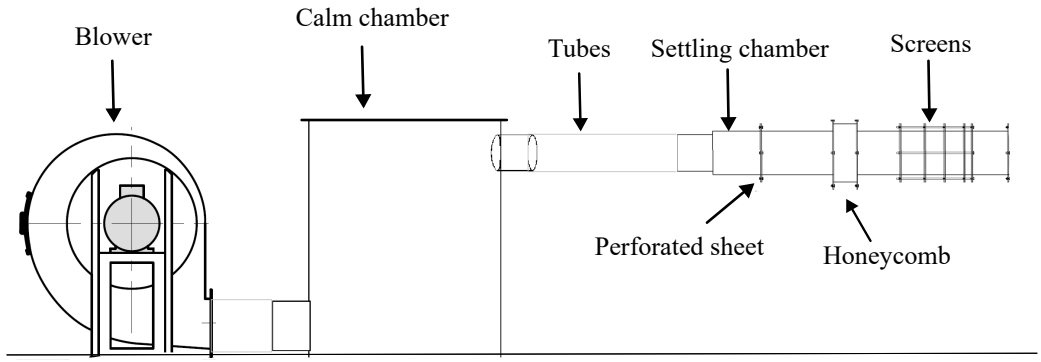

Figure 3.3: PAT layout.

Considering PAT circuit shown in Fig.3.3, it is composed of [18], [5]:

- Calm chamber: to reduce the effect of strong fluctuations due to the blower;
- Tubes: to connect the calm chamber with the modular part;
- Modular part: is a series of modules with different flow conditioners and in sequence there are:
  - Settling chamber: to increases homogeneity of the fluxes coming from the tubes;
  - Perforated sheet with $\beta = 0.58$: reduces turbulence and improve honeycomb performance;
  - Honeycomb with $\beta = 0.9669$: reduces cross-stream fluctuations and aligns the flow;
  - Screens: five screens with $\beta = 0.605$, $\beta = 0.588$, $\beta = 0.588$, $\beta = 0.595$ and $\beta = 0.595$ are used to damp streamwise component of turbulence.

β is the porosity and for the perforated sheet and screens and it is defined as:

$$\beta = \frac{A_{free}}{A_{tot}}. \tag{3.13}$$

where A_{free} is the cross section area where fluid can pass and A_{tot} is the whole cross section. For the honeycomb the definition is different:

$$\beta = \left(1 - \frac{d}{M}\right)^2. \tag{3.14}$$

where d is the thickness of the cell walls and M is the side length of the cell. Further details on the geometry of all the flow conditioners and the spacing between them is reported in [18] and [5].

The computation of the losses can be divided into:

- Distributed losses: for the tubes, settling chamber and straight sections within flow conditioners;
- Concentrated losses: for all the flow conditioners and inlet and outlet of tubes.

For distributed losses, where friction is the main contribution, it has been used the so called Chen equation [11]:

$$\frac{1}{\sqrt{c_f}} = -2\log_{10}\left[\frac{\epsilon}{3.7065D} - \frac{5.0452}{Re_D}\log_{10}\left(\frac{1}{2.8257}\left(\frac{\epsilon}{D}\right)^{1.1098} + \frac{5.8506}{Re_D^{0.8981}}\right)\right]. \tag{3.15}$$

c_f is the skin friction coefficient whereas the ratio ϵ/D is the relative roughness of the surface defined with the equivalent hydraulic diameter D, that is the ratio between the cross section area and its perimeter. Re_D is the Reynolds number defined with the hydraulic diameter i.e. $Re_D = UD/\nu$. Instead, for each flow conditioners specific formulas have been used to find K [18], [5].

Since this evaluation is in any case an approximation of the real operative conditions, instead of recomputing all the losses of PAT, the following argument is applied:

$$\Delta Q = \frac{Q - Q'}{Q'} = \frac{0.6529 - 0.6258}{0.6258} \sim 4.3\%. \tag{3.16}$$

where Q' is the flow rate reported in [18]; but since the geometry of the PAT is unchanged from [18] the equation can be rewritten as:

$$\Delta Q = \frac{Q - Q'}{Q'} = \frac{UA_{tot} - U'A_{tot}}{U'A_{tot}} = \frac{U - U'}{U'} = \Delta U. \tag{3.17}$$

where U is the average cross section velocity, and analogously for the Reynolds number, so $\Delta Q = \Delta U = \Delta Re$. Thus, as approximation, the losses coefficients already found in [18] could be considered almost equal to the ones that would have been computed for the present case, since the variation in conditions is enough small.

Adding all the contributions, the total coefficient for the PAT segment is $K_{PAT} = 2.33$.

3.1.3.2 Convergent losses

The contraction adds distributed losses due to friction and concentrated losses due to flow separation. In general for curvilinear contractions, as it is the present case, the main contribution can be limited to friction [21], [7]. So, the computation of the pressure losses reduces to the integral:

$$\Delta p = \int_0^{l_c} \frac{\rho}{2} c_f(x) \frac{U^2(x)}{D(x)} dx. \tag{3.18}$$

where $U(x)$ is the local average cross-section velocity, $D(x)$ the local equivalent diameter and $c_f(x)$ the local equivalent friction coefficient that can be estimated using Eq.(3.15). Actually this relation can be further simplified assuming an average $\bar{c}_f$ equal to the average of the the skin friction coefficient at the inlet and outlet of the contraction so, the losses coefficient can be written as:

$$K_c = \frac{\Delta p}{\frac{\rho}{2} U_i^2} = \bar{c}_f \int_0^{l_c} \frac{1}{D(x)} \frac{U^2(x)}{U_i^2} dx = \bar{c}_f \frac{l_c}{D_i} \int_0^1 \frac{D_i^5}{D^5(x)} d\left(\frac{x}{l_c}\right). \tag{3.19}$$

where D_i is the inlet equivalent diameter and from continuity there is $U(x)^2 = U_i^2 D_i^4 / D^4(x)$. Then, recasting K_c to test section condition by substituting D_i with D_0, that is the equivalent diameter for the test section, the equation becomes:

$$K_{c_0} = \bar{c}_f \frac{l_c}{D_0} \int_0^1 \frac{D_0^5}{D^5(x)} d\left(\frac{x}{l_c}\right). \tag{3.20}$$

and the integral is found to be always lower than 1 and generally is approximated as 0.32 [7], [16]. Thus, the final law is:

$$K_{c_0} = 0.32 \bar{c}_f \frac{l_c}{D_0}. \tag{3.21}$$

Moreover, since the cross section is not circular, the following corrective coefficient should multiply K_{c_0} [21]:

$$K_{nc} = 1.1 - 0.1 \frac{\bar{h}}{w}. \tag{3.22}$$

where $\bar{h}$ is the average height of the contraction thus, $K_{c_0} = K_{nc} K_{c_0}$. In Tab.3.3 are reported the values of the parameters obtained for the present case. The value of surface roughness ϵ used is the one for plastic material, in particular an general value for PLA since the contraction will be made 3D printed.

3.1.3.3 Channel losses

The computation for the losses in straight duct, as it is the case for the channel segment, follows the same procedure used for the convergent [7]. Eq.(3.15) is used to estimate the friction coefficient and in this case the value of ϵ refers to Plexiglass since the channel will be made of this material. The losses coefficient will have the total length of the channel L and it is already referred to test section, indeed the whole channel is considered the test section. In Tab.3.4 are listed all the relevant values found.

Table 3.3: Contraction parameters (computed considering same air properties as for the optimization algorithm).

Parameter	Value
l_c	180 mm
w	450 mm
h_i	180 mm
CR	4.5
$\bar{h}$	110 mm
D_i	257 mm
D_0	73.5 mm
ϵ	$2 \cdot 10^{-5}$ m
K_{nc}	1.7056
K_{c_0}	0.0151

Table 3.4: Test section parameters (computed considering same air properties as for the optimization algorithm).

Parameter	Value
L	2700 mm
w	450 mm
h	40 mm
D_0	73.5 mm
ϵ	$2 \cdot 10^{-6}$ m
K_{nc}	1.0911
K_{ts}	0.6642

3.1.3.4 Total K factor

In order to find the total losses of the circuit, all the coefficients must be referred to a common condition, typically the test section condition. Thus, the local coefficient can be recasted in the following way:

$$K_{local_0} = \frac{\Delta p_{local}}{\frac{1}{2}\rho U_0^2} = \frac{\Delta p_{local}}{\frac{1}{2}\rho U_i^2}\frac{U_i^2}{U_0^2} = K_{local}\frac{A_0^2}{A_i^2}. \tag{3.23}$$

where subscript "0" stands for test section condition and "i" for local inlet condition. Except for the coefficient of the channel that is obviously referred to test section condition and the contraction that is already converted, PAT coefficient must be converted. As proved above the local value must be simply multiplied by the cross section area ratio $(A_0/A_{PAT})^2$, giving $K_{PAT_0} = 0.518$. Moreover, since no diffuser will be used at the outlet of the test section must be considered a concentrated loss with coefficient equal to 1.

Adding all the contribution the total value is $K_{total} = K_{PAT_0} + K_{c_0} + K_{ts} + 1 = 2.17$. So, the total pressure drop due to the circuit losses is:

$$\Delta p_{total} = K_{total}\frac{1}{2}\rho U_0^2 = 2.17 \cdot \frac{1}{2} \cdot 1.225 \cdot (36.27)^2 = 1771 Pa. \tag{3.24}$$

and the power dissipated:

$$P_d = \Delta p_{total} Q = 1771 \cdot 0.6529 = 1.156 kW \tag{3.25}$$

These conditions are found to lie within the operational limits of the centrifugal blower already installed for the PAT [18], [5], and the parameters of the test bench are confirmed.

3.1.4 Wind tunnel final layout

Once the design part has been completed, a CAD modeled is designed. This allowed to find a solution to the requirements on the usage of this facility, in particular the optic accessibility, since measures will be done mainly with PIV technique, and facility handling, in other words compatibility with PAT structure and ease of maintenance.

In order to grant the best visibility, it has been decided to make the whole channel of Plexiglass. Instead of other transparent plastic material such as polycarbonate, Plexiglass is more rigid and transparent, and its properties are more stable in time. These reasons justified the selection of this material. Then, to facilitate the maintenance of the channel the structure components must be removable. To account for this it has been designed with 3 modules, each 900 mm long, that can be connected in sequence. Two for the developing of the flow exiting from the convergent and a final one that is the effective test section in which the actuator is placed. A metal structure has the function of sustaining the channel and keeping at a height sufficient for placing around all the PIV equipment. The layout of the three modules is the same. Two side walls are connected with the upper and lower walls with bolts; the connection is designed such that is sealed without filler material and the inner side of each wall has no contact with the external structure. In this way, the corners end exactly straight without fillets that could limit the visibility near the walls as shown in Fig.3.4. The test section has the same shape of the other previous modules and the only difference is the door on the upper wall as can be seen in Fig.3.5. The door dimensions allow to install actuators with a maximum size of 390 mmx300 mm with the longer side along the cross stream direction. From the outer part to the inner part exposed to the flow, it is left an empty space of 20 mm that can host cables and supports of the actuator, in this way the height of the device can be modified independently with respect to the channel wall.

The contraction shown in Fig.3.6 instead, is 3D printed and made of PLA. This solution has two main advantages: first, complex geometries can be realised with good quality and its cheaper than making it of Plexiglass, since no optical access is required for this component. A disadvantage of 3D printing is that a surface pattern is left on the object due to the process of deposition of the filament, so to minimize this effect, the building of the object is done in such a way to minimize the material used as support for the object and to have layers growing in direction parallel to the flow direction. After printing all the component are sanded to reduce even more the surface defects.

The complete layout can be seen in Fig.3.7.

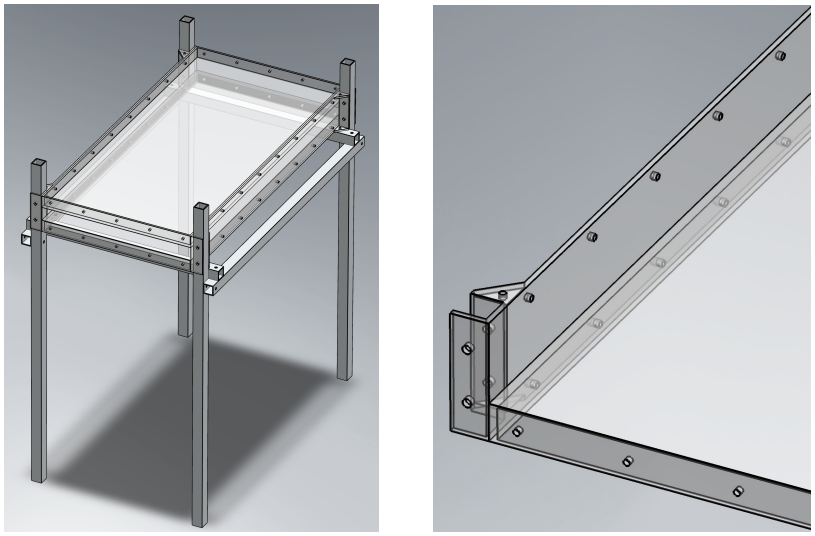

(a) (b)

Figure 3.4: One of the two module for the devoloping region (a), and view of the corner between the side and lower wall (b).

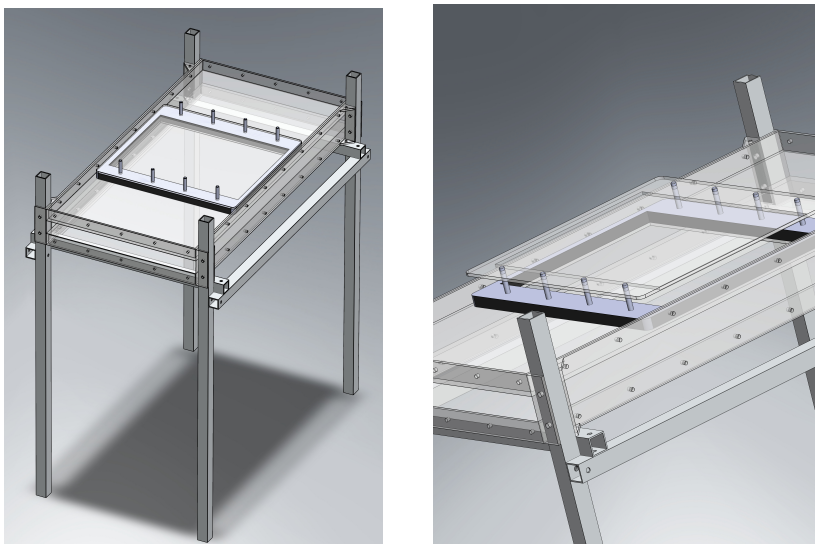

(a) (b)

Figure 3.5: Test section module (a), and view of the door (b).

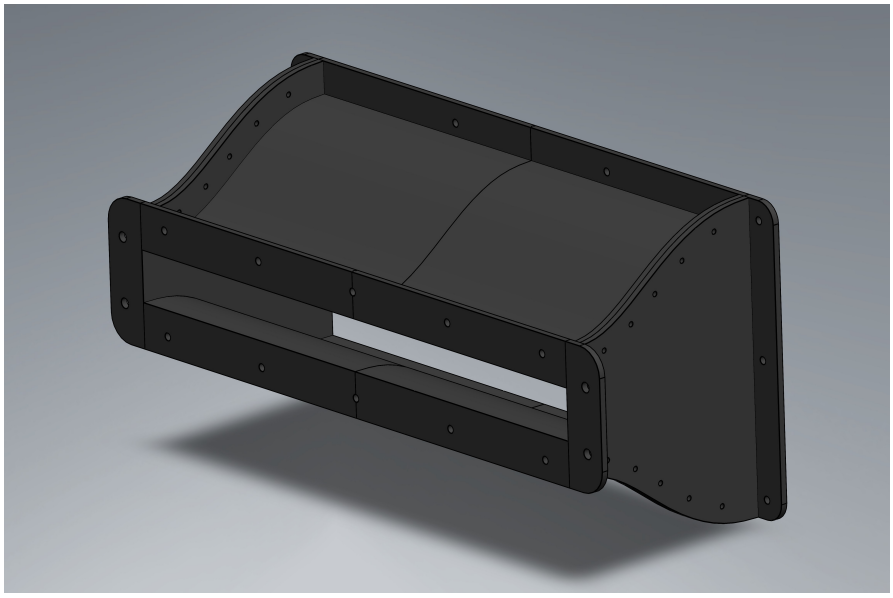

Figure 3.6: Convergent with all the printed blocks joint together.

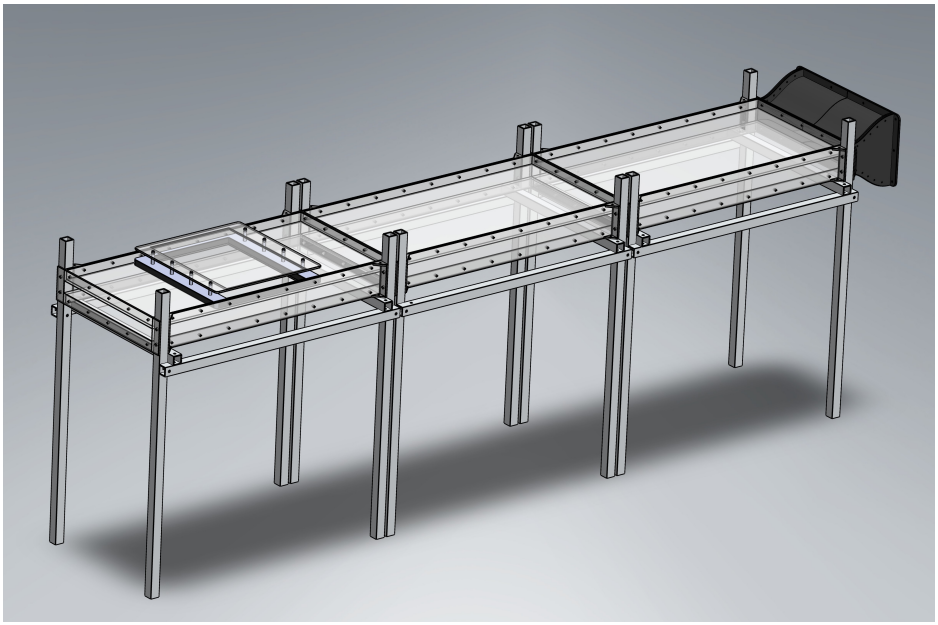

Figure 3.7: Complete layout of the channel with the convergent; it can be appreciated the modularity of the structure.

Chapter 4

Experimental background

4.1 Flow measurements

Dealing with plasma actuators requires more attention than other devices for flow control. As already discussed in the introduction of the previous chapter, common instruments such as Pitot tube and hot wire anemometer can interfere with the actuator. Pitot tube made of plastic materials cannot be damaged by accidental discharges by the actuator but, they can affect the electric field because they could accumulate charges. Hot wire probe instead can not be used in the proximity of the actuator otherwise an accidental discharge can seriously damage or even destroy the probe and the other electrical equipment connected to it, in other words the probe can become the local, not insulated, ground of the actuator circuit.

If forces and moments generated by the device are the only aim of the measurements, balances are the best option, since they are the only instrument that is not interacting directly with the actuator [26] and the only issue is the sensitivity, since the force generated is of the order of mN.

But if flow quantities such as the velocity field, are the topic of the investigation, the best way to obtain these data is with optical techniques and indeed both LDV and PIV are widely used [26]. Schlieren imaging is used too, in general to see the fast transient of the shock wave propagating from the actuator, but no velocity field information can be extrapolated. The problem with optical techniques that need seeding as tracer particles, is that these particles flowing in the neighbourhood of the actuator can be ionized and then they interact with the electric field generated by the device. For this reason oil based and disco smoke should be avoided, while TiO_2 and silica micro balloons are recommended [26].

Since the test bench proposed in this work is designed for obtaining more information as possible about the tested actuator, PIV technique has been selected as the most proper for this aim.

In the following sections, a general introduction about particle image velocimetry, and electrical measurement technique is given. In the next chapter the discussion will be focused on the selected set up that will be explained in detail.

4.1.1 PIV measurements

Particle image velocimetry is an indirect measurement technique, since respect to other technologies such as hot wire anemometry and the pitot probe which measure fluid properties, it finds the velocity field by exploiting sequences of images of tracer particles injected in the flow [37]. The vector fields obtained can be or two dimensional and two component vector, in the case of planar PIV, or two dimensional but three component with stereoscopic PIV or even three dimensional and three component with tomographic PIV. In any case three elements are necessary: tracer particles to be injected into the flow, instruments for recording image sequences and a light source for proper illumination of the seeding.

Since the type of PIV used in this work is the planar one, the following discussion will be focused only on this type.

Regarding tracer particles two characteristics are fundamental: first the dynamic behaviour when they are moving in the flow and second the light scattering properties. To estimate the time response of seeding, a straightforward way is to consider spherical particles of density ρ_p and diameter d_p, and assuming not too high Reynolds number, the Stokes' drag law can be used to estimate the velocity of the particle and so compute the velocity difference with the flow:

$$U - U_p = d_p^2 \frac{(\rho_p - \rho)}{18\mu} \frac{dU}{dt}. \tag{4.1}$$

where ρ is the fluid density, μ the fluid viscosity. Then by integrating this differential equation in time, if $\rho_p \gg \rho$ the solution is an exponential decaying law from which the following time constant can be found:

$$\tau_p = d_p^2 \frac{\rho_p}{18\mu}. \tag{4.2}$$

it is clear that the best tracer is the one that, in relation to the fluid in which is injected, it has the minimum τ_p that means that it reaches the velocity equilibrium with the fluid in a shortest time. In order to decrease this time the only possible way is to decrease d_p and ρ_p. The problem of decreasing particles' diameter is that this reduces the light scatter requiring more powerful light sources and as will be explained later on, too small particles can affect negatively also the computation of the velocity field.

As light source usually laser is preferred to standard light sources since it is required more energy to illuminate properly the particles. Among the several types of laser the most common are the two listed in Tab.4.1. Both Nd:YAG and Nd:YLF have the so called Q-switch that is a device that allows to generate concentrated light pulses, in this way the energy output is higher than a continuous beam.

Table 4.1: Most representative laser types (taken from [16]).

Laser type	**Wavelengths** $[nm]$	**Pulse energy** $[mJ]$	**Repetition rate**	**Pulse duration** $[ns]$
$Nd:YAG$	1064/532	$50 - 400$	$5 - 100\ Hz$	10
$Nd:YLF$	1054/527	$5 - 30$	$1 - 10\ kHz$	150

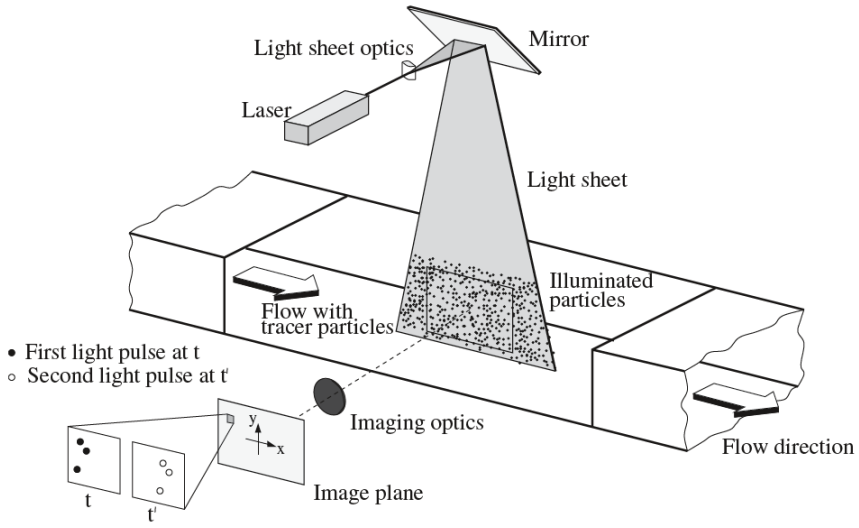

Figure 4.1: PIV layout example (taken from [37]).

Then lenses and mirrors are used to modify the beam shape and direction to obtain the desired laser sheet. Theoretically the mid plane of the laser sheet is the plane for which the optics of the image recording device are focused. A sketch of this set up is shown in Fig.4.1. For image recording nowadays high-speed digital cameras are used and CCD (Charge Coupled Device) or CMOS (Complementary Metal Oxide Semiconductor) are the two main sensor technologies.

The working principle beyond PIV measures, is the comparison of pairs of images taken in sequence at small time instants between them. Displacements are retrieved by cross-correlating the so called interrogation areas of each image pair. Indeed both the first and second image of the pair is divided into small regions whose shape is usually square from a minimum of 16 pixels side to 128 pixels and the position of these interrogation areas must be the same in the first and second image. Actually must be clarified that the shape of the interrogation area can vary depending on the flow considered and could be even not square if the flow present strong gradients in a specific direction. The cross-correlation map $R(x, y)$ can be computed in the following way:

$$R(x,y) = \sum_{-k}^{k} \sum_{-l}^{l} I(x,y) I'(x+k, y+l). \tag{4.3}$$

where $I(x, y)$ and $I'(x, y)$ are the image intensity in the image location in pixel unit (x, y). Basically the second interrogation area is shifted of integer position (k, l). The correlation map obtained as shape $(2k + 1)$x$(2l + 1)$ where $l = 1/4n$ and $k = 1/4m$, being mxn the shape of second frame interrogation area intensity [37]. In Fig.4.2 is shown the described process.

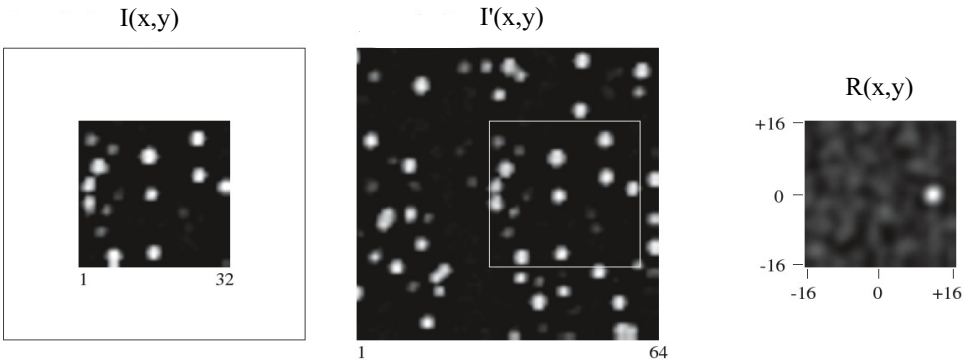

Figure 4.2: Example of cross-correlation samples with $m = n = 64$. The white spot in the $R(x, y)$ map corresponds to the correlation maximum (taken from [37]).

Once computed the correlation map $R(x, y)$, then the maximum location correspond to the (k,l) integer shifts that yields the best match of the intensity pattern of I in I'. By repeating this process for all the interrogation areas in which the image has been divided at the end it is found the whole displacements field. Considering nxn interrogation area, the computational cost of the direct cross-correlation done as Eq.(4.3) is of the order of $O[n^4]$, while implementing cross-correlation in frequency domain with fast Fourier transform, dramatically reduces the computational cost to $O[n^2 \log_2 n]$. The main limitations with FFT-based correlation are the aliasing and the bias error and they are both related to the assumption of spatial periodicity of the intensity map. The correlation map in the case of FFT-based has shape nxn, if the detected maximum is outside the the correlation map, meaning that the displacement $d > N/2$, aliasiang error occurs and the maximum is folded back inside the correlation map giving a wrong displacement. Instead bias error is due to the fact that as displacement increases, less intensity data are available for correlation, so the uncertainty of the estimated peak location in the correlation map increases. To reduce aliasing the best strategy is to increase the interrogation area, even if padding with zeros can raise noise at high frequency, whereas to limit bias error proper windowing can be applied to the correlation map. Windowing consists of applying a weighting function to the correlation map value, several functions have been studied with different results depending on the flow case [3]. From displacement fields then is possible to convert directly to velocity by just multiplying the entire field as follows:

$$(U, V) = \left(\frac{p_x k}{M \Delta t}, \frac{p_x l}{M \Delta t} \right). \tag{4.4}$$

where M is the magnification ratio and p_x the pixel dimension of the camera optics and Δt is the so called interframe time, that is the interval between the pair of images.

Magnification M is directly linked with the particle diameter that strongly affects the correlation results, and the effective diameter that is detected by the camera sensor can be written as:

$$d_\tau = \sqrt{(Md_p)^2 + d_{diff}^2}. \tag{4.5}$$

where diffraction contribution can be approximated to:

$$d_{diff} = 2.44 \frac{f}{D_a}(M+1)\lambda. \tag{4.6}$$

with f the focal length, D_a the aperture diameter of the camera optics and λ the laser wavelength. Diffraction contribution is higher when there is the combination of small M and small particles, and this condition is called diffraction limited and affects particle with $d_p \leq 1\ \mu m$ which is the case of seeding generated by smoke machines. The diffraction manifests its effect with a specific pattern, the Airy disk, that are concentric circles with decreasing brightness around the particle. Sharper particle images can be obtained by increasing D_a and this improve correlation but with too larger D_a lens aberrations effects increase as well. Moreover a minor contribution in d_τ is due to the loss of focus which is increasing linearly with $D_a M$ [3] so D_a again must be not too large.

Said δz_0 the laser sheet thickness, the image density N_I can be defined as:

$$N_I = \frac{C\delta z_0 p_x m n}{M}. \tag{4.7}$$

C is the number of particles per volume. N_I represents the average number of particles per interrogation area and for PIV analysis a minimum threshold is of at least $N_I = 10$. The average number of matching particles per interrogation area can be estimated considering three contribution to the fractional losses of these particles pairs [37], [16]:

- Particle loss due to in-plane motion F_I: particles exit from the interrogation area field of view and the match is lost, and said $(\Delta_x, \Delta_y, \Delta_z)$ the mean displacements and D_x and D_y the side lengths of the interrogation area, F_I can be approximated to:

$$F_I = \left(1 - \frac{\Delta_x}{D_x}\right)\left(1 - \frac{\Delta_y}{D_y}\right). \tag{4.8}$$

- Particle loss due to out-of-plane motion F_O: Δ_z makes particles exit from the illuminated region of thickness δz_0 and they disappear within the interrogation area:

$$F_O = 1 - \frac{\Delta_z}{\delta z_0}. \tag{4.9}$$

- Particles matching loss due to displacement gradients F_Δ: considering small displacement gradient inside the interrogation area boundaries, this term could be estimated as:

$$F_\Delta = exp\left(-\frac{2}{3}\frac{a^2}{d_\tau^2}\right) \tag{4.10}$$

where a is the mean variation of displacement in the interrogation area, approximated as $a = M|\Delta_{max} - \Delta_{min}|\Delta t$. $|\Delta_{max} - \Delta_{min}|$ is a rough estimation of the strongest displacement gradient that could be present along one of the two directions parallel to the interrogation area sides so $d(\Delta)/dxD_x$ or $d(\Delta)/dyD_y$. F_Δ contribution is important when parameter a reaches the dimension of d_τ, meaning that the difference in displacements approaches the length of the particles' diameter. The effect on the cross-correlation map is that the highest peak is broadening and lowering and multiple peaks appears. This makes difficult to find the true peak to get the correct average displacement.

The average number of correlated particle pairs is the product $N_I F_I F_O F_\Delta$. Fig.4.3 collects the results of different PIV analysis done on synthetic images. Valid vectors refers to displacement that are correct according to the validation algorithm chosen. Indeed several techniques can be used as well as specific combinations or ad hoc solutions [37]. As general rule a measurement can be considered acceptable if at least more than 80% of the vector field is valid [16]. Considering a standard cross-correlation algorithm, if the number of valid vector is lower than the threshold, two actions can be done: modify the interrogation area size and adjust the magnification M and the interframe time Δt but for example increasing the interrogation area can lead to an undesired spatial averaging of the field. On the other hand, if all the vector field is valid, it could be useful to modify D_x, D_y, M and Δt to increase for example the spatial resolution by decreasing D_x and D_y.

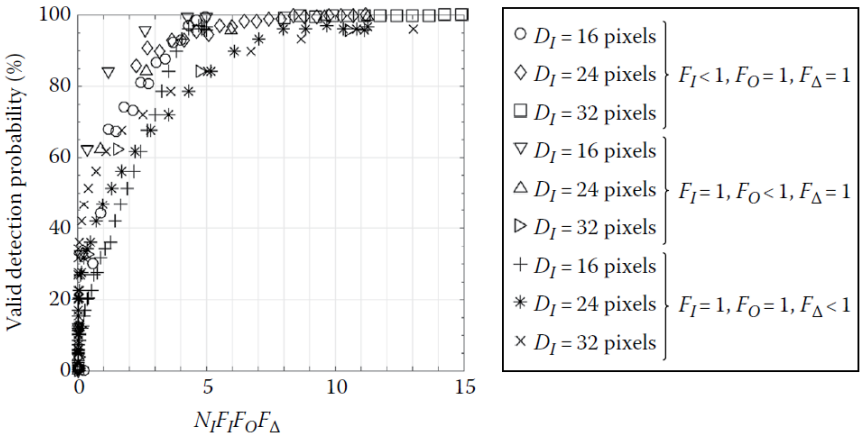

Figure 4.3: Valid vectors percentage as function of $N_I F_I F_O F_\Delta$ for different combination of $D_I = \sqrt{D_x D_y}$ and F_I, F_O and F_Δ. Results of PIV analysis on synthetic images (taken from [16]).

About the value of the displacement, regardless it is valid or not, usually it is performed the so called sub-pixel estimation. The principle behind is that the correlation map that is computed is discrete, this implies that the x and y displacement are integer values introducing an uncertainty of $\pm 1/2$ *pixel*. To reduce it, a local interpolation of the correlation map is performed and the peak position of the extrapolated surface will be regarded as the effective displacement. Typically Gaussian based surfaces are used as estimators since the intensity of particle resembles

a Gaussian surface and mathematically, the cross-correlation of a Gaussian function is still a Gaussian. The simplest function is the three-point Gaussian estimator:

$$x_0 = i + \frac{\ln R(i-1,j) - \ln R(i+1,j)}{2(\ln R(i-1,j) - 2\ln R(i,j) + \ln R(i+1,j))}. \tag{4.11}$$

$$y_0 = j + \frac{\ln R(i,j-1) - \ln R(i,j+1)}{2(\ln R(i,j-1) - 2\ln R(i,j) + \ln R(i,j+1))}. \tag{4.12}$$

so basically the peak location (x_0, y_0) is found interpolating separately along x and y direction respectively.

Regarding the PIV algorithms, several variations have been proposed to the standard procedure. The aim in this case is to obtain more information at fixed experiment parameters namely M, Δt. This can be achieved by increasing vector field resolution and to do so interrogation areas should be minimized since overlapping should be limited to maximum 75%. The problem of reducing D_x and D_y is that the displacements should be within $D_x/4$ and $D_y/4$ both for direct cross-correlation and FFT-based correlation, this fact puts a lower bound to the minimum area size. To avoid this, image deformation has been introduced. Basically they area class of iterative algorithm that deform the image of a pair by the displacement field found at the previous iteration, as iterations go on the displacement field is updated until the detected displacements go below a threshold or the maximum iteration number is reached. The correlation peaks will shift to the center of the correlation map since the deformation of the images progressively increase their matching. The displacements found at iterations after the first are small so the interrogation area can be safely reduced increasing further the resolution. Two main schemes can be used:

- **Window offset**: each interrogation area is shifted of the displacement found at previous iteration; the concept is sketched in Fig.4.4a;
- **Window deformation**: each interrogation area is continuously deformed by interpolating the displacement field for each pixel as illustrated in Fig.4.4b .

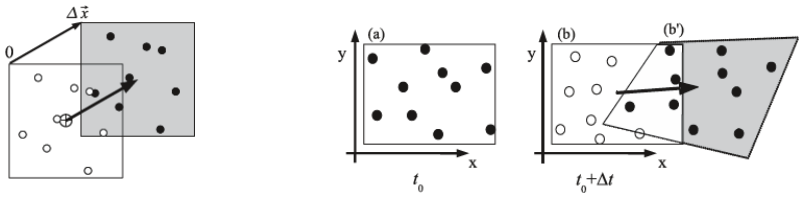

(a) (b)

Figure 4.4: Window offset of a particle pattern (a). Window deformation technique (b): "a" particle pattern at first timestep, "b" second snapshoot of the image pair and "b'" the deformed particle pattern that resemble pattern in "a" (taken from [16]).

The iterative procedure is basically a predictor-corrector method. Before applying the deformation field, it must be validated and filtered [37]. Moreover if window

deformation is applied, typical interpolation scheme of the displacement field are the bilinear and the B-spline; B-spline of order above 3^{rd} are better even if the computational effort is higher [37]. Instead, since the image is deformed the image must be interpolated too and also in this case B-splines are the best solution [6]. The problem with iterative algorithms is the instability that can raise by the transfer function of the interrogation area. The oscillating behaviour of displacements has a spatial wavelength of $\lambda_{uns} \simeq 2/3D_I$ and yields a wavy pattern. This can be compensated by applying a proper windowing function to the correlation map. Window deformation algorithm are usually multi-pass and multigrid meaning that the interrogation area and overlapping are modified at each pass that corresponds to an iteration of the image deformation; for standard PIV analysis 3 passes are enough to convergence [37].

Adaptive algorithms instead, modify the interrogation area according to local conditions of the flow [40]. Indeed the multigrid approach, especially without image deformation, can lead to poor correlation signal since the optimization of the interrogation area is satisfied on a average sense [37].

A suitable method to evaluate the correlation signal, is by checking the signal to noise ratio (SNR). Several definition are present in literature but, one of the most implemented is the primary peak ratio [45]:

$$SNR = \frac{max\{R\}_I}{max\{R\}_{II}} \tag{4.13}$$

where $max\{R\}_I$ is the correlation peak and $max\{R\}_{II}$ the second tallest correlation peak values.

The planar PIV set-up used will be shown in section 3.4 together with the complete set-up.

4.2 Electrical measurements

As anticipated in the introduction of this chapter, in order to fully characterize the behaviour of a plasma actuator it is fundamental both to quantify the actuation effect on the flow as well as the power consumed to obtain this effect.

Since for this work only DBD actuator will be tested, all the following description will refer only on electrical measurement techniques used for this type of actuator.

The main problem of measuring electrical parameters of a working actuator is that it is required a fast acquisition system capable of reaching frequencies of the order of GHz. Oscilloscope connected to high voltage probe can be used to measure voltage and the impedance of the cables used to connect the probe to the instrument can modify the output value of the measure.

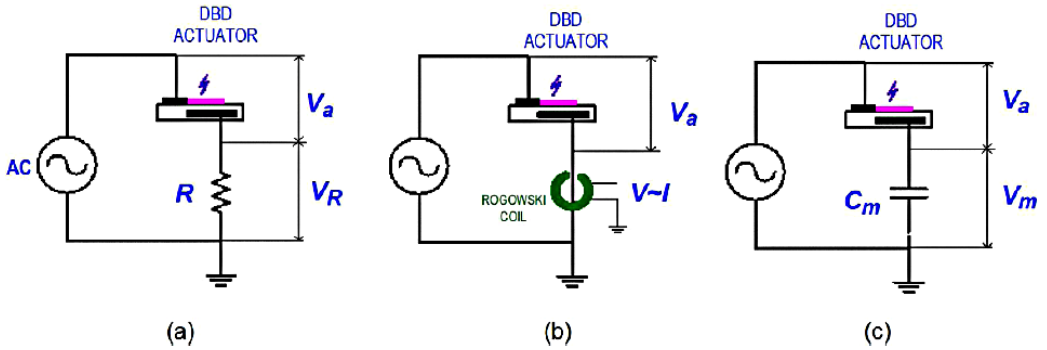

Figure 4.5: Shunt resistor scheme (a). Rogowski coil scheme (b). Shunt capacitor scheme (c) (taken from [26]).

In Fig.4.5 are represented the schemes for the three principal strategies used to measure current. With shunt resistor, current is found by Ohms law $I(t) = V_R(t)/R$ and $V_R(t)$ is measures. With Rogowski coil, inductance effect is exploited. Indeed the coil wrapped around the ground cable reacts to the magnetic field generated by the inner conductor and a current can be measured between coil's ends. The frequency bandwidth of Rogowski coil goes only from 100 Hz to 500 Hz so high frequencies discharges and low frequencies capacitive components can not be resolved. Hall current sensor can be used instead of Rogowski coil since its bandwidth is of the order o 100 MHz [26]. The instantaneous power consumed by the actuator is simply the product of the current by the applied voltage. Another way to derive the power without having to measure the current is by using the shunt capacitor circuit. In this way the accuracy problem due to limited frequency resolution are minimized. The working principle is the following, the instantaneous charge accumulated in the capacitor is:

$$Q_M(t) = C_M V(t)_M. \tag{4.14}$$

with C_M being the capacitance. The current flowing in the actuator is equal to the one flowing in the capacitor so:

$$I_M(t) = \frac{dQ_M(t)}{dt} = C_M \frac{V_M(t)}{dt}. \tag{4.15}$$

so the instantaneous power is:

$$P(t) = V_a(t)I_M(t) = V_a(t)C_M\frac{V_M(t)}{dt}. \tag{4.16}$$

The total power can be computed by integrating Eq.(4.16) over a sufficiently large number of cycles [27]. The average power per cycles can be computed in the following way:

$$P_{av} = \frac{1}{n_c}\sum_{1}^{n_c} f\int_0^T V_a(t)C_M\frac{V_M(t)}{dt} = \frac{f}{n_c}\sum_{1}^{n_c}\int_0^T V_a(t)dQ_M. \tag{4.17}$$

where $f = 1/T$ is the AC frequency used to power the actuator and n_c is the number of cycles. Eq.(4.17) is basically the average of the area enclosed in the so called Lissajous curve. An example of this graph can be seen in Fig.4.6.

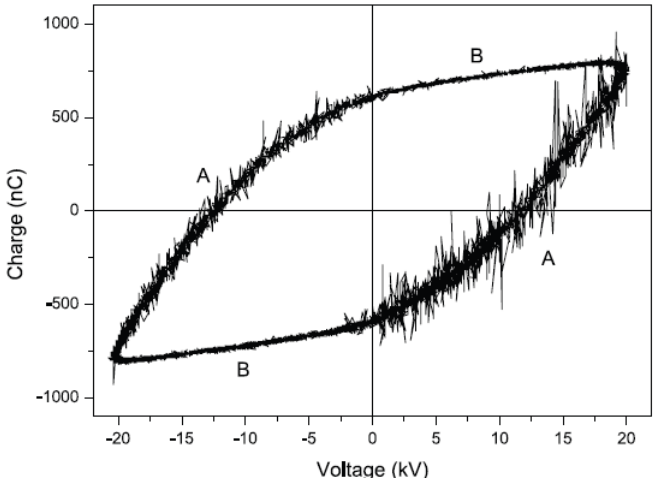

Figure 4.6: Example of Lissajous graph $Q_M(V_a)$ of a surface discharge; discharge is ignited in quadrants denoted with "A" (taken from [26]).

The shunt capacitor technique is preferable compared to the previous one, because the charge related to all microdischarges accumulates in the capacitor and so can be effectively integrated in time. This relaxes the requirement of fast acquisition rates and increases the accuracy. Moreover, the circuit is extremely simple and cheap. Care must be taken when selecting the capacitor, indeed the capacitance should be enough high to avoid saturation.

Chapter 5

Experimental set-up

The full set-up includes, together with the wind tunnel, also the electrical equipment necessary for plasma generation and control. In Tab.5.1 are listed all the test bench components shown in Fig.5.1.

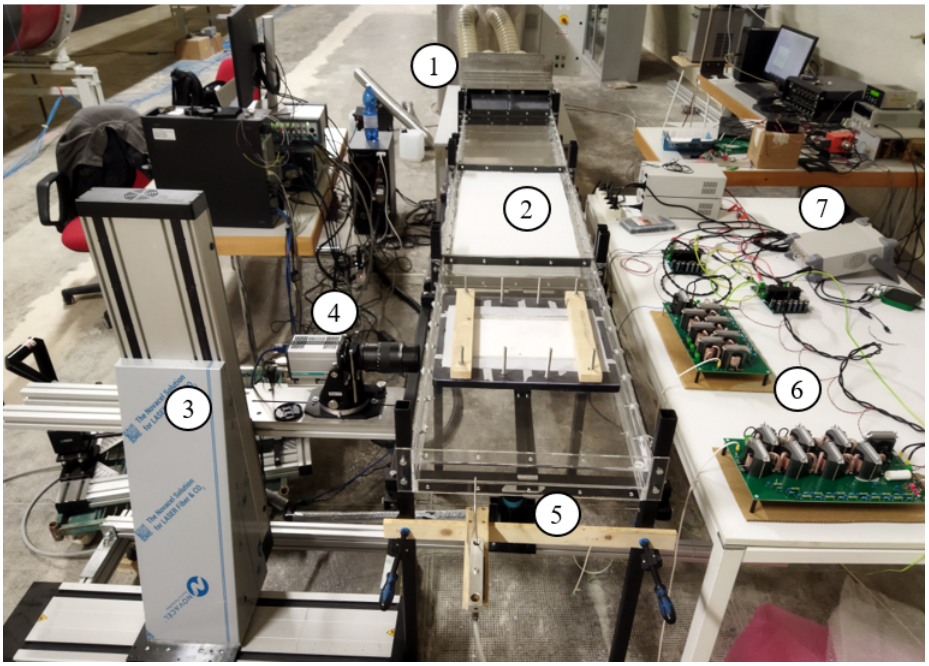

Figure 5.1: Complete test bench set-up.

Table 5.1: Components of the set-up in Fig.5.1 with relative description.

Id number	**Component**	**Features**
1	PAT	Centrifugal blower and flow conditioners.
2	Channel	Plexiglass wind tunnel.
3	Traversing system	Movement allowed along y and z directions.

4	HiSense Zyla camera	The sensor can record images of 2560x2160 *pixel*.
5	Laser head	Wavelength of 532 *nm*; the laser head can be moved along a rail.
6	MiniPuls 4	2 MiniPulse 4 systems are used to independently control the generation of plasma.
7	Wave generator	Wave generator used to generate the base signal for the Minipulse.

For all the PIV analysis it has been used as seeding a disco smoke of type L, with average particle diameter of the order of few microns.

5.1 Actuator's specifications

For this work it has been used a DBD actuator with teflon as dielectric material. The actuator dimensions are 210 *mm*x297 *mm* and the thickness of the dieletric material is 0.6 *mm*. The electrodes, made of gold plated copper, are aligned parallel to the smaller side.

Figure 5.2: View of the exposed electrodes of the DBD actuator used during the tests. The black frame around the actuator is the mask used to block it inside the test section door.

The exposed electrodes have a width of 3 *mm* whereas the ground electrodes have a width of 9 *mm*. In this configuration, each ground electrode is within the upper electrode of two different phases and no gap is present. The two phases of

the exposed electrodes can be controlled independently via the two MiniPuls. The side of the actuator where ground electrodes are present, has been entirely insulated with commercial silicone as can be seen in Fig.5.3 and no back plasma formation has been observed. In Fig.5.2 is shown the described actuator.

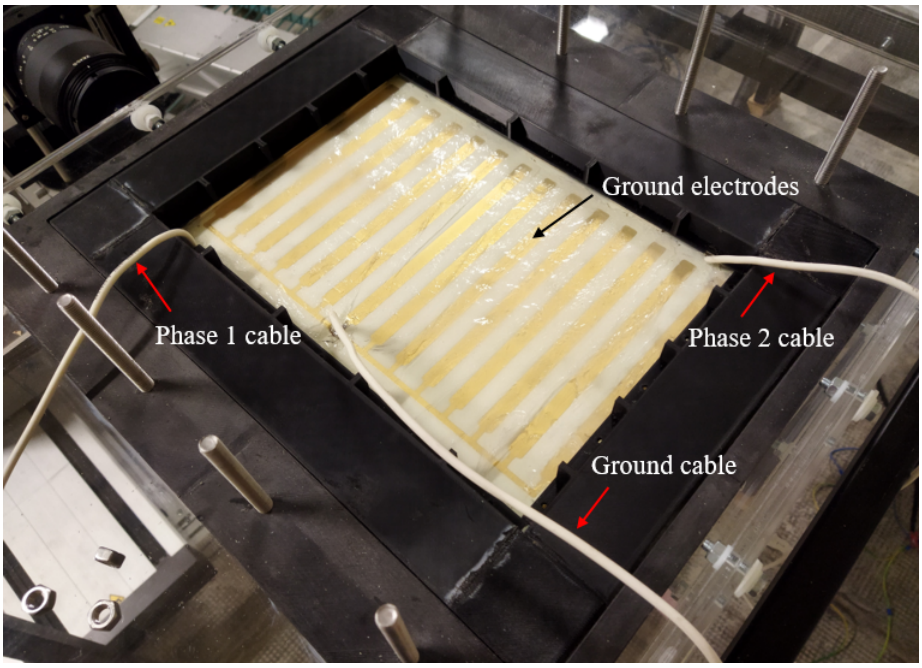

Figure 5.3: View of the back side of the DBD actuator used during the tests.

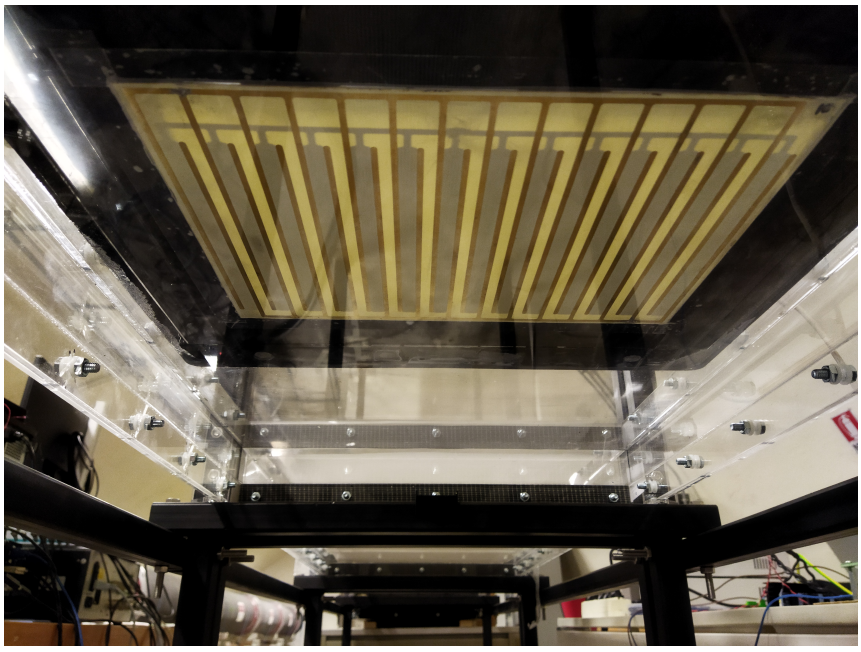

Figure 5.4: View of the exposed side of the DBD actuator installed in the test section.

The actuator is installed in the wind tunnel with the electrodes parallel to the streamwise direction of the flow in the channel as can be seen in Fig.5.4; the flow induced by the actuator will be directed spanwise. This configuration has been chosen in order to test the wall normal jet actuation and the oscillating wall mode. Details will be given later in the next chapter.

5.2 PIV calibration

The PIV calibration has been performed with a movable target on which it has been attached a graph paper. The procedure is the following and is the same for all the analyses. The target is placed at the centerline of the channel and the camera's plane of focus is reached by adjusting both the camera optics and via the traversing system. Once the plane of focus coincides with the target the laser sheet is moved to coincide with the target plane. The calibration is then performed and the coordinates system is found by defining the centerline of the target as $y = \delta$ the half width of the channel. Fig.5.5 shows the image acquired for the calibration.

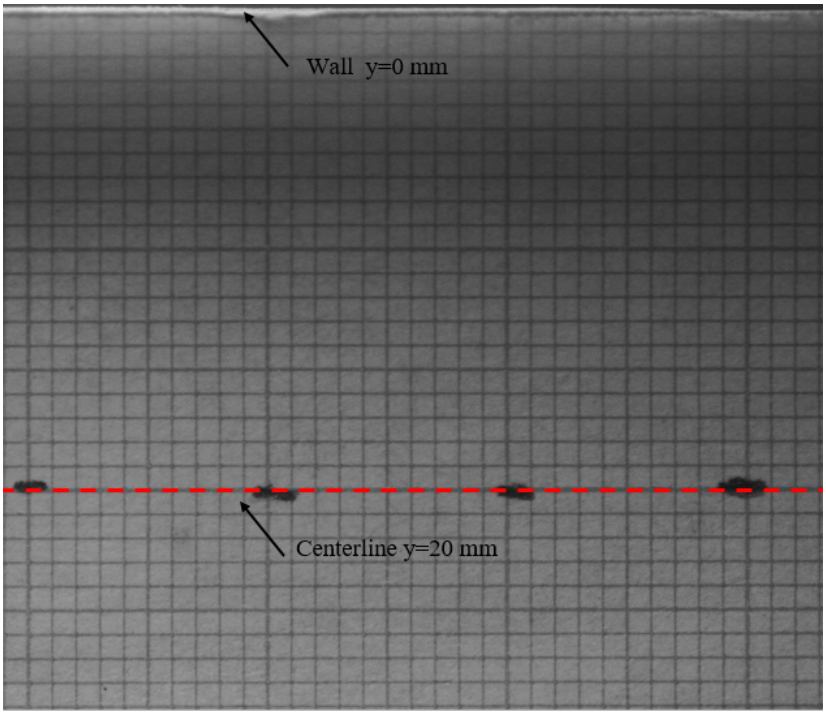

Figure 5.5: Image used for PIV analysis calibration; red dashed line, the channel's centerline used as reference for the coordinates system.

As it will be explained later, the PIV measurements were performed at the exit of the contraction along the spanwise direction and at the centerline and in the middle of the test section. For the first case, the calibration was performed only at the centerline and then for the other positions, the laser head and the camera were moved together using the traversing system. In the chapter about the discussion of the results, there will be explained the uncertainties in the estimation of the walls'

position. It must be specified that the coordinates system in the first analysis is the equal to the one sketched in Fig.2.12, i.e. with $y = 0$ at the bottom wall, whereas in the second case $y = 0$ is located in the upper wall, that is the side where is installed the actuator.

Chapter 6

Results

After building the whole structure, the experimental investigation has been divided in two part:

1. Characterization of the performance of the wind tunnel at different regimes;
2. First attempt of velocity field measurements with plasma actuator installed and activated at the design working condition of the wind tunnel.

For these first tests, the power consumption data about the plasma actuator are not available.

6.1 Wind tunnel performance characterization

Before proceeding with any measurement in the test section it is fundamental to analyse the behaviour of the wind tunnel. This allows to identify design errors that could invalidate the data acquired during following experiments, and correct them with proper solutions. In the case of the present project, they were established two key aspects to be verified:

- Velocity profile near the exit of the contraction along the vertical direction and downstream spanwise profile;
- Velocity profile and flow statistics along the vertical direction at the mid-plane of the test section.

6.1.1 Contraction characterization

Planar PIV technique has been used to analyse the velocity vector field at position $2h$ from the exit of the convergent. In Tab.6.1 are reported the parameters for all the wind tunnel working condition investigated. There are also indicated the frequencies of the inverter used to control the centrifugal blower. As can be noticed, the frequency step is decreased moving towards higher values. This has been chosen in order to increase the resolution near the design working point of the plant, i.e. centerline mean velocity of $\sim 40\ m/s$. The reference system for the coordinates of any position is the same and equal to the one sketched in Fig.2.12.

Table 6.1: Plant parameters and PIV parameters for the contraction characterization.

Blower inverter frequency $[Hz]$	**Laser trigger rate** $[Hz]$	U_0 $[m/s]$	Δt $[\mu s]$
10	13	8.68	36
20	13	17.4	17
30	13	23.8	13
35	13	27.8	11
40	13	34.1	9
45	13	36.7	9
50	13	39.9	8

The centerline velocities listed in the third column are found with a Pitot tube mounted at the exit of the wind tunnel and fixed at the mid-plane of the channel, i.e. position $(y, z) = (\delta, 0)$. For each change in spanwise position the U_0 has been checked and ambient temperature, pressure and density were registered. The variation of density was within 1%, with the ambient pressure being constant during the measurements. With averge temperature being $T_{amb} = 297\ K$ and ambient pressure $p_{amb} = 98265\ Pa$, the air density is $\rho = 1.15\ kg/m^3$. From differential pressure measurements Δp, obtained with the Pitot tube, the axial component of velocity can be computed as:

$$U = \sqrt{\frac{2\Delta p}{\rho}}. \tag{6.1}$$

U_0 is the mean value of U over 40 s of acquisition. The information gained with U_0 has been used to compute the interframe time Δt by applying the so called "1/3 rule". This means that considering a standard 32x32 *pixels* interrogation area for the PIV analysis, the interframe time within a image pair, is such that the average displacement is equal to 1/3 of the interrogation side length in pixel units. After some first trials, it has been chosen to relax the constraint on Δt to allow a better reconstruction of the field near the walls, where the velocity intensity can be even one order of magnitude lower than the centerline speed. With the magnification used, 1 $pixel = 0.0279698\ mm$ thus, the field of view is equal to 71.6 mmx60.4 mm, but the ROI used reduces the height to the one of channel, i.e. 40 mm. For the analysis has been chosen a interrogation area of 32x32 *pixels* with 50% of overlap, and with the selected magnification this corresponds to more or less 2 vectors per millimeter. The number of samples necessary to have a stable avarage field has been evaluated considering first 400 samples. By setting the threshold to 5% for the mean standard deviation normalized with the centerline velocity, it has been found that 200 samples for each case would have been a reasonable compromise between memory for the storage of the data and results quality. The velocity field has been measured at 6 spanwise location, $z = [0h, 1h, 2h, 3h, 4h, 4.875h]$. The velocity profile of the average x-component is taken at $x = 2h$ from the contraction exit. Normalized profiles are presented below for each inverter frequency analysed.

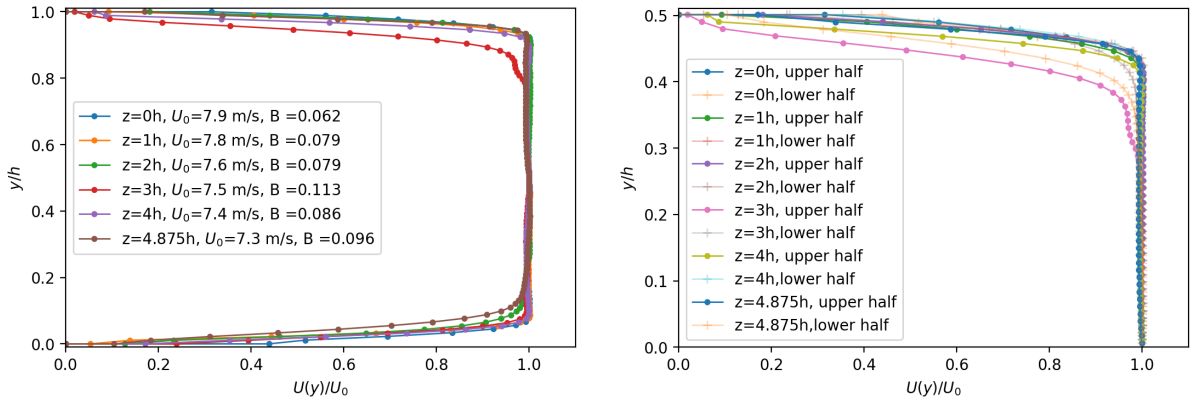

(a) Full profile.

(b) Upper and lower half profile.

Figure 6.1: Normalized velocity profiles at inverter frequency of 10 Hz.

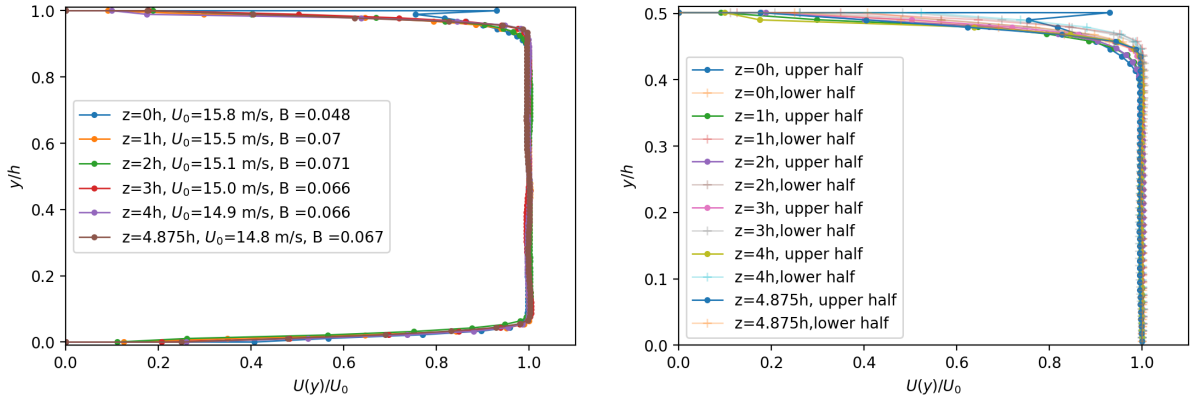

(a) Full profile.

(b) Upper and lower half profile.

Figure 6.2: Normalized velocity profiles at inverter frequency of 20 Hz.

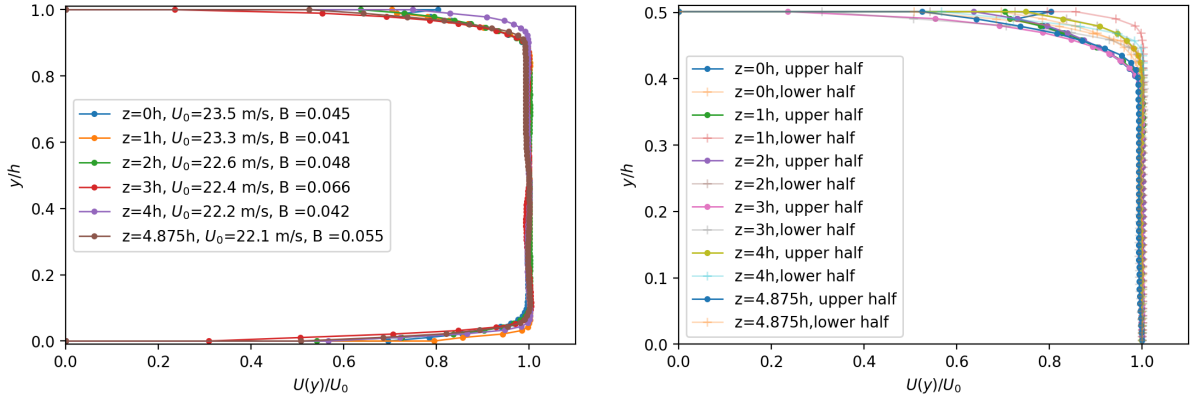

(a) Full profile.

(b) Upper and lower half profile.

Figure 6.3: Normalized velocity profiles at inverter frequency of 30 Hz.

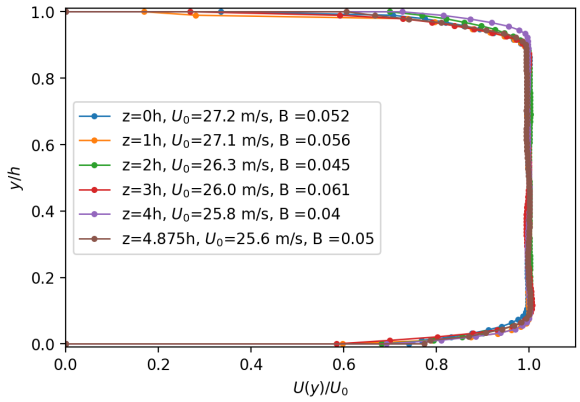

(a) Full profile.

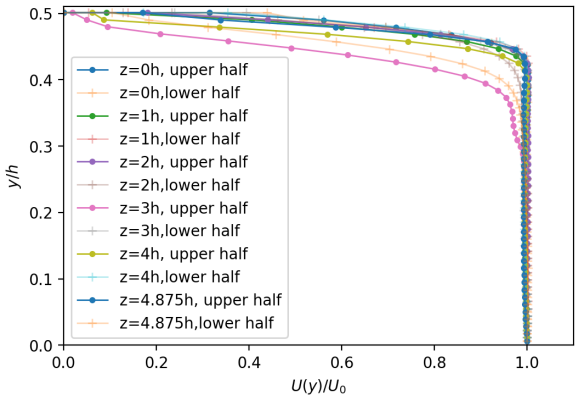

(b) Upper and lower half profile.

Figure 6.4: Normalized velocity profiles at inverter frequency of 35 Hz.

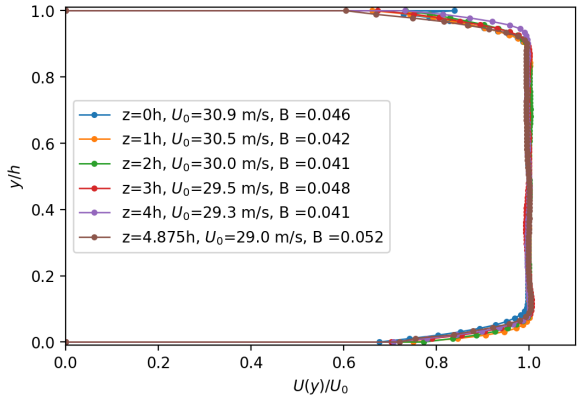

(a) Full profile.

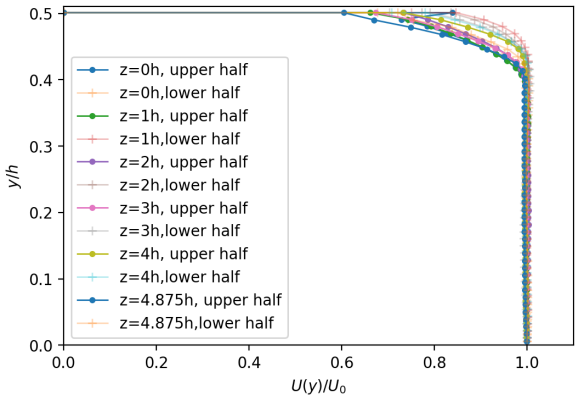

(b) Upper and lower half profile.

Figure 6.5: Normalized velocity profiles at inverter frequency of 40 Hz.

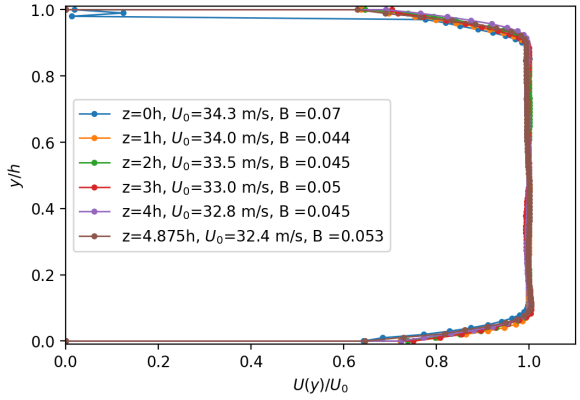

(a) Full profile.

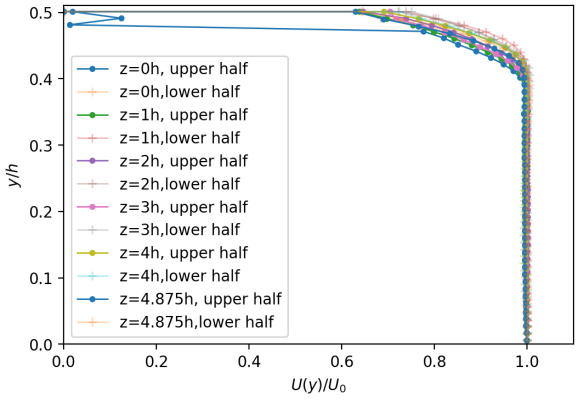

(b) Upper and lower half profile.

Figure 6.6: Normalized velocity profiles at inverter frequency of 45 Hz.

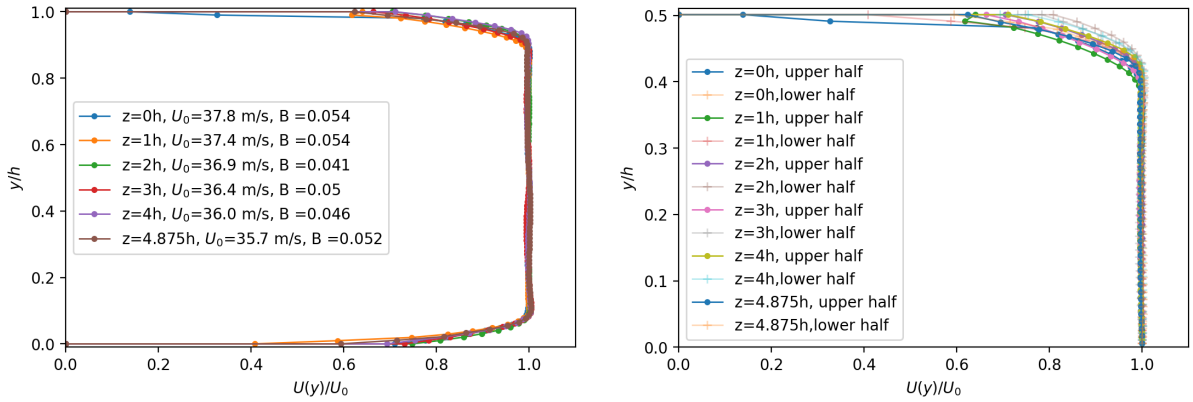

(a) Full profile.

(b) Upper and lower half profile.

Figure 6.7: Normalized velocity profiles at inverter frequency of 50 Hz.

From Fig.6.1 to Fig.6.7 are shown the vertical velocity profiles obtained with PIV measurement. Instead, to analyse the centerline spanwise profile, the velocity has been derived from Pitot tube measurements. The spanwise step has been halved from h to $h/2 = \delta$, with respect to PIV stations, to increase the resolution. Moreover, not only the positive side but the whole profile has been sampled.

Since the measurements for the vertical profile and the spanwise profile have been done in different days, the ambient conditions are different leading to slight changes in the measured quantities. Indeed the new conditions are $T_{amb} = 296.4\ K$, $p_{amb} = 100630\ Pa$ which corresponds to $\rho = 1.18\ kg/m^3$.

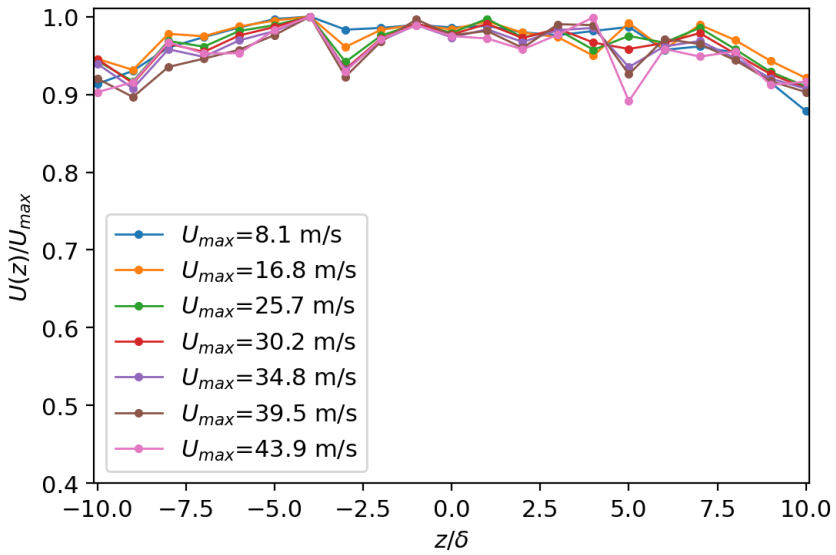

Figure 6.8: Normalized spanwise profile at inverter frequencies: 10 Hz, 20 Hz, 30 Hz, 35 Hz, 40 Hz, 45 Hz and 50 Hz. The velocities reported in the legend are the maximum velocity at these frequencies.

6.1.2 Vertical velocity profile at test section mid-plane

Again with PIV technique, the half vertical velocity profile has been analysed at the mid-plane of the test section. In this case only half channel has been considered in order to double the spatial resolution. The new field of view is 34.8 mmx29.4 mm and the ROI is such that the upper side coincides with the upper channel wall and the lower side is at the center of the channel. This test is performed at only one speed, $U_0 = 41.18\ m/s$, which is the design working point velocity. Again it has been used an interrogation area of 32x32 *pixels* with 50% of overlap, this requires an interframe time $\Delta t = 4\ s$ and the first vector is at 218 μm which corresponds to $y^+ \simeq 22$ according to the values used for designing the channel in Tab.3.2. All statistical moments have been computed using a total of 400 samples. Normalized velocity profile is shown in Fig.6.9.

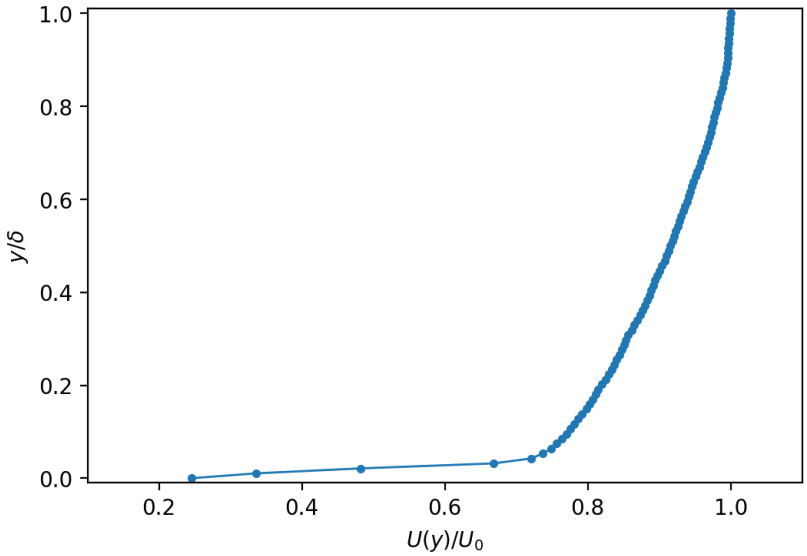

Figure 6.9: Normalized half velocity profile along vertical direction.

Moreover the shear stress $\tau(y)$ has been derived in the following way:

$$\tau(y) = \nu\rho\frac{d\langle U\rangle}{dy} - \rho\langle uv\rangle. \tag{6.2}$$

with $\rho = 1.15\ kg/m^3$ and $\nu = 1.546 \cdot 10^{-5}\ m^2/s$. The values of the Reynolds stress are known at each vector position, instead the viscous term is computed with a first order finite difference scheme. The values of $\tau(y)$ are found at intermediate locations between two subsequent points. Thus the Reynold stress is linearly interpolated at these points. The implemented formula is:

$$\tau(i) = \nu\rho\frac{\langle U\rangle\left[i+\frac{1}{2}\right] - \langle U\rangle\left[i-\frac{1}{2}\right]}{dy} - \rho\frac{\langle uv\rangle\left[i+\frac{1}{2}\right] + \langle uv\rangle\left[i-\frac{1}{2}\right]}{2}. \tag{6.3}$$

The result can be seen in Fig.6.10.

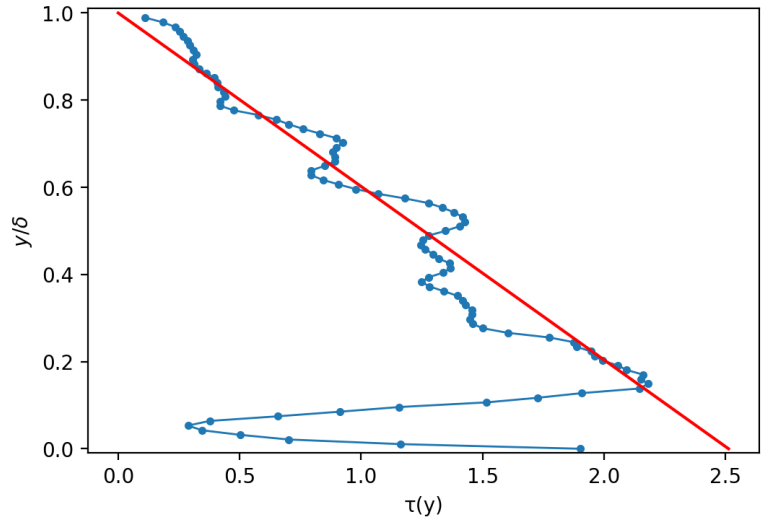

Figure 6.10: $\tau(y)$ with normalized positions in blue; analytical solution in red, obtained with estimated τ_w.

Since no pressure measurements are available at the wall location, and the first vector is already in the buffer layer, one way to estimate the inner scales δ_ν and u_τ is by deriving τ_w exploiting the analytical solution [20]. Thus, τ_w can be written as:

$$\tau_w = \tau(y)\frac{1}{1-\frac{y}{\delta}}. \tag{6.4}$$

Since $\tau(y)$ presents some scatter, the value of τ_w considered, is the average of the values obtained for $0.2 < y/\delta < 1$.

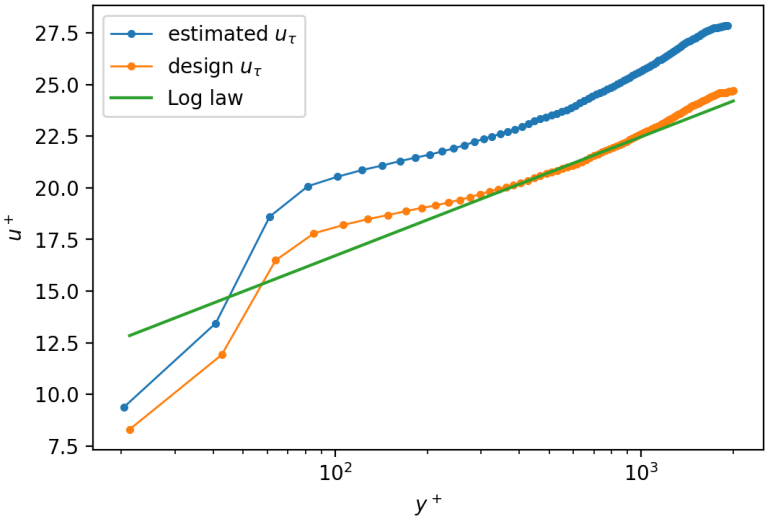

Figure 6.11: Comparison of velocity profile scaled with different inner scales: inner scales estimated with τ_w method in blue, inner scales with method used during design in orange; log law Eq.(2.28) with $k = 0.4$ and $B = 5.2$ in green.

This yields a value of $\delta_\nu = 10.5\ \mu m$ and $u_\tau = 1.49\ m/s$ instead of the design values of $\delta_\nu = 10\ \mu m$ and $u_\tau = 1.67\ m/s$. In Fig.6.11 is reported the velocity profile in inner scale units normalized with estimated and design values of the inner scales. Since the normalization with the design values yields a better agreement with the log law, these values were used for the normalization of all the statistical quantities. In Fig.6.12, Fig.6.13 and Fig.6.14 are shown respectively: the variance of u, v and the Reynolds stress in inner units.

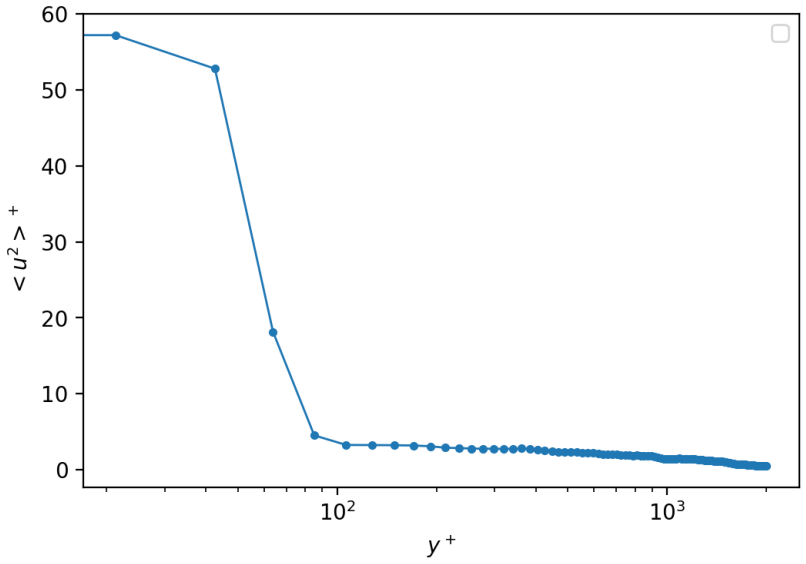

Figure 6.12: Variance of u component scaled with inner scales.

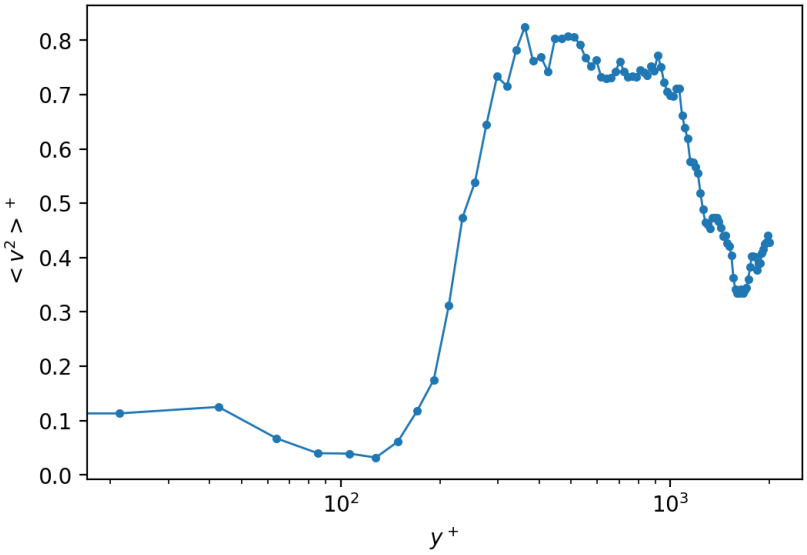

Figure 6.13: Variance of v component scaled with inner scales.

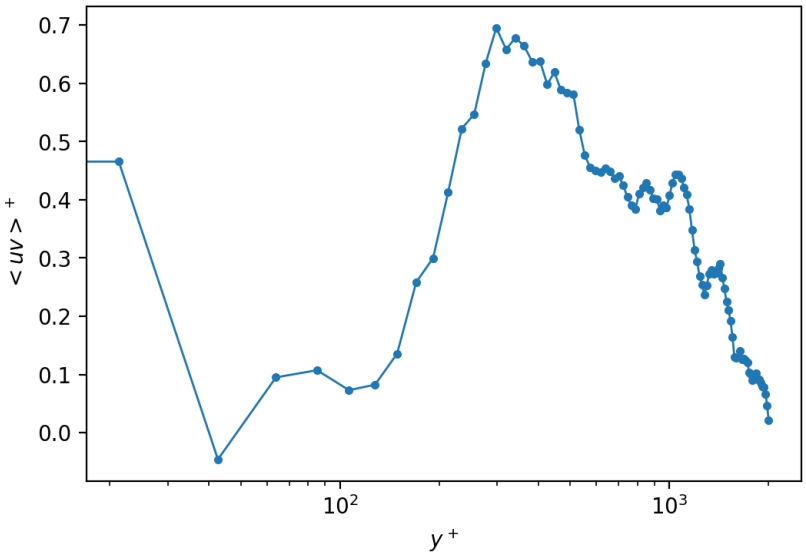

Figure 6.14: Reynolds stress scaled with inner scales.

6.2 Velocity field measurements with plasma actuator

Completed the flow measurements with the actuator disabled, then it has been switched on and four actuation modes were tested:

- Wall normal jet: the two phases are synchronized to push at the same time, this creates wall normal jets that go away from the wall over the ground electrodes, whereas they go towards the wall over the exposed electrodes. Considering the present configuration, this wall normal jets generate pairs of counter-rotating vortices along the streamwise direction;
- Oscillating wall mode at 5 Hz: the two electrodes are pushing with a phase shift of π, with modulation frequency of 5 Hz. The effect is to generate an oscillating spanwise component that mimics the behaviour of an oscillating wall;
- Oscillating wall mode at 50 Hz: same as previous case but the modulation frequency is raised to 50 Hz;
- Oscillating wall mode at 100 Hz: modulation frequency is 100 Hz.

For all this cases the base signal to power the two phases of the plasma actuator, is a square wave of frequency 12 kHz and $V_{p-p} = 13\ V$ provided by the wave generator. With this inputs, the MiniPuls controlling this actuator were able to generate a sinusoidal voltage output of $V_{p-p} = 6\ kV$ at 12 kHz. These measurements were performed by analysing the signal output provided by a dedicated port of the MiniPuls connected to an oscilloscope. The signal for the modulation of the oscillating wall modes is given by another independent wave generator and also for this case, a square wave has been chosen with $V_{p-p} = 4\ V$ and a duty cycle of 45%.

The field established during actuation has been analysed at the same condition presented before for the analysis of the velocity profile in the test section. Below are reported the normalized velocity profile, $\tau(y)$, and again the velocity profile, u and v variance and the Reynolds stress normalized with inner scales with the same procedure presented before. The inner scales estimated with the previous methods are listed in Tab.6.2. For all these graphs, it has been reported again the case without actuation as reference for the actuated cases.

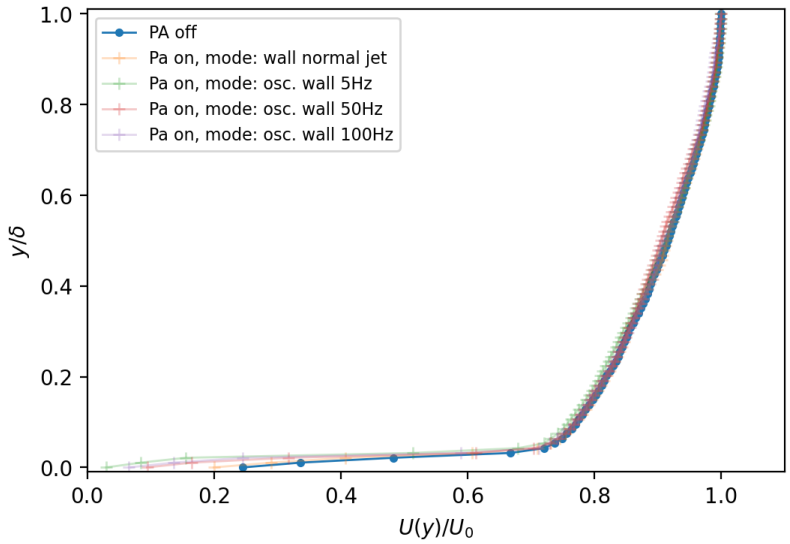

Figure 6.15: Normalized half velocity profile along vertical direction for different actuation modes.

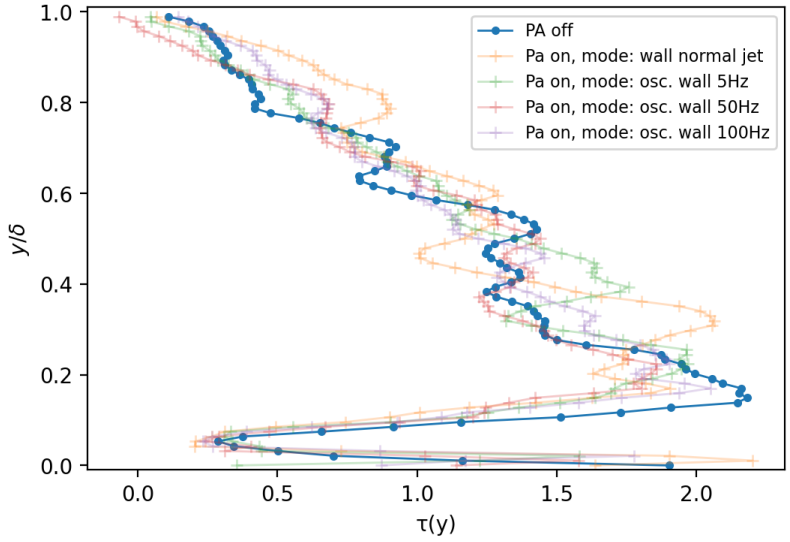

Figure 6.16: $\tau(y)$ with normalized positions for different actuation modes.

Table 6.2: Inner scales estimated values for different actuation modes.

Actuation mode	U_0 $[m/s]$	u_τ $[m/s]$	δ_ν $[\mu m]$
Pa off	41.18	1.46	10.5
Pa on, mode: wall normal jet	41.09	1.54	10.0
Pa on, mode: osc. wall 5 Hz	41.03	1.52	10.2
Pa on, mode: osc. wall 50 Hz	40.90	1.46	10.6
Pa on, mode: osc. wall 100 Hz	40.55	1.49	10.4

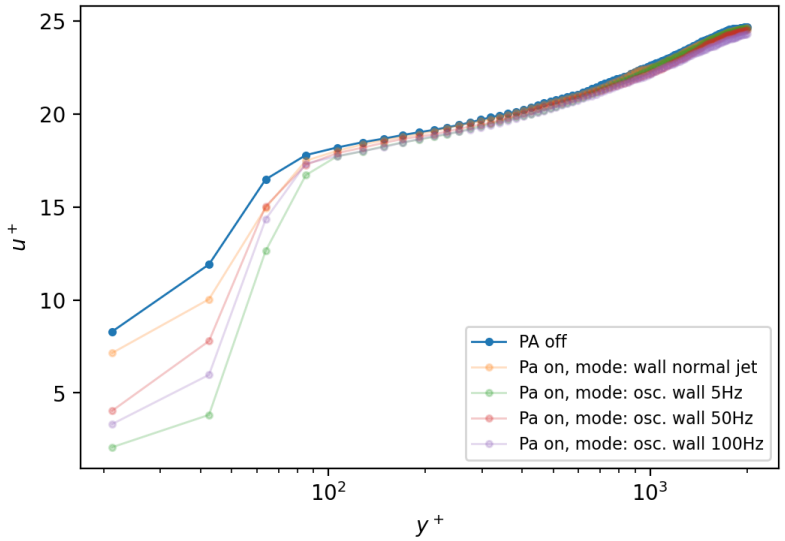

Figure 6.17: Velocity profile scaled with inner scales for different actuation modes.

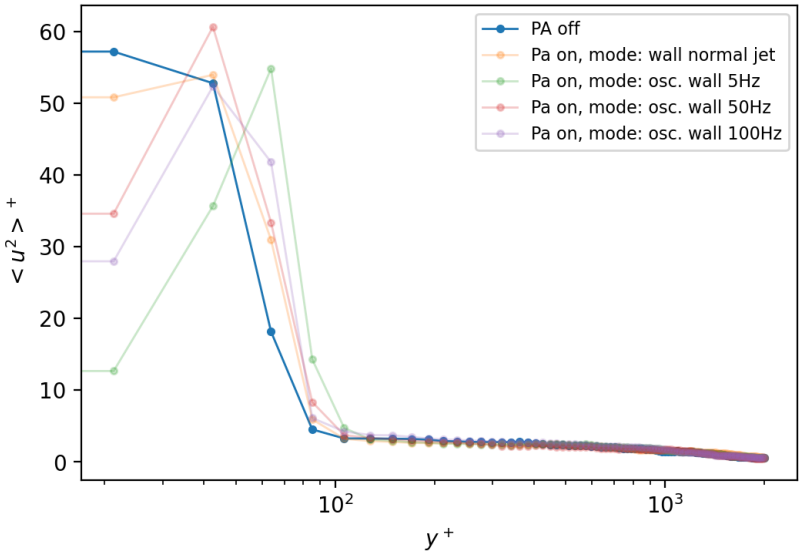

Figure 6.18: Variance of u component scaled with inner scales for different actuation modes.

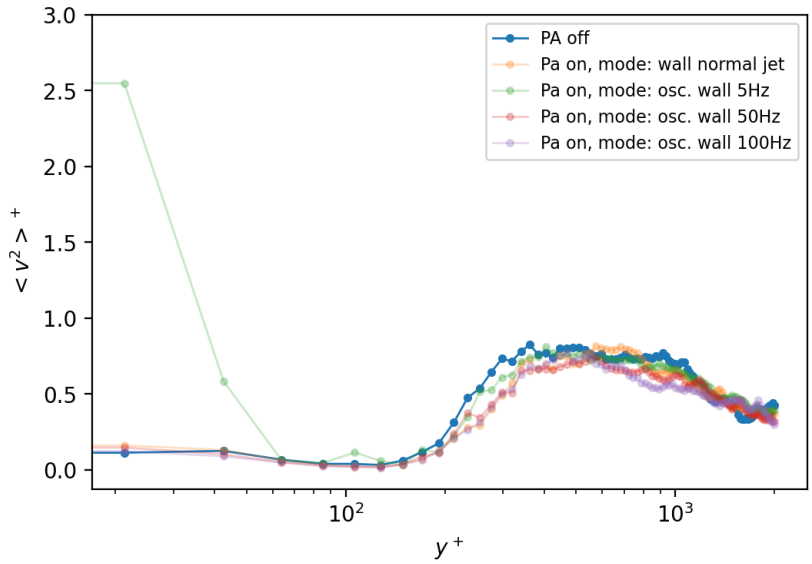

Figure 6.19: Variance of v component scaled with inner scales for different actuation modes.

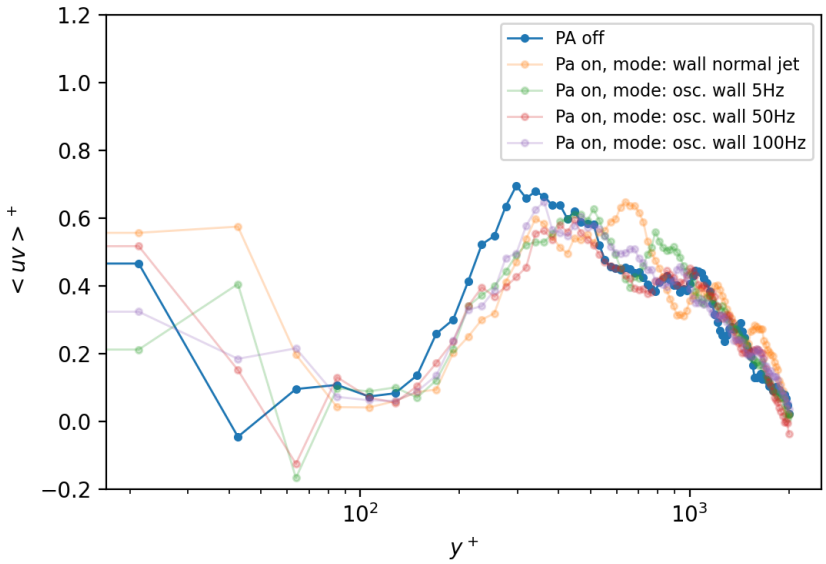

Figure 6.20: Reynolds stress scaled with inner scales for different actuation modes.

Chapter 7

Discussion of the results

The analysis carried to characterize the performance of the wind tunnel shows that the average velocity profile along the vertical direction has a top-hat shape at all the analysed spanwise locations. To quantify the regime of the flow it has been used a blockage factor defined as:

$$B = \frac{2\delta_1^*}{h} = \frac{1}{h}\int_0^h \left(1 - \frac{U(y)}{U_{max}}\right) dy = 1 - \frac{\bar{U}}{U_{max}}. \tag{7.1}$$

where δ_1^* is the displacement thickness. According to this definition values of B around 0.05, indicate that the profile is turbulent. Except for low wind tunnel speed, i.e. inverter frequencies below 20 Hz, the values of B found for all the profiles at different spanwise positions appears to be around the target value of 0.05. All these values are reported in the legends of figures from Fig.6.1 to Fig.6.7. Fig.6.1 shows an unexpected deviation of the upper half profile at position $z = 3h$ with respect to the other locations. Moreover, in general as can be observed for all the following profiles it can been noticed that the upper half of each profile, presents higher scatter and this is quite clear when the two halves are reported together. On the other hand as velocity increases, the profile symmetry is more stable, this can lead to infer that maybe, flow instabilities can be in part responsible of this behaviour. The symmetry of the profiles is even more evident when it is plotted as the normalized difference between the two halves.

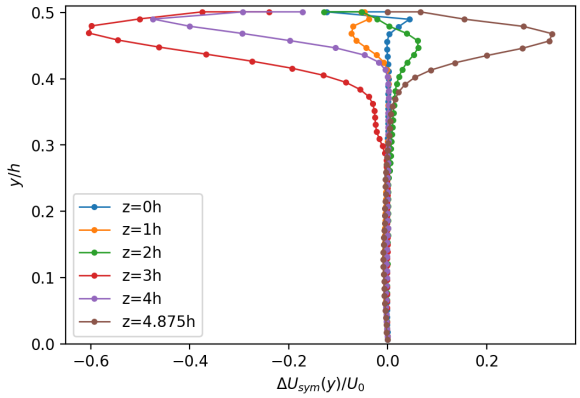

(a) Inverter frequency of 10 Hz.

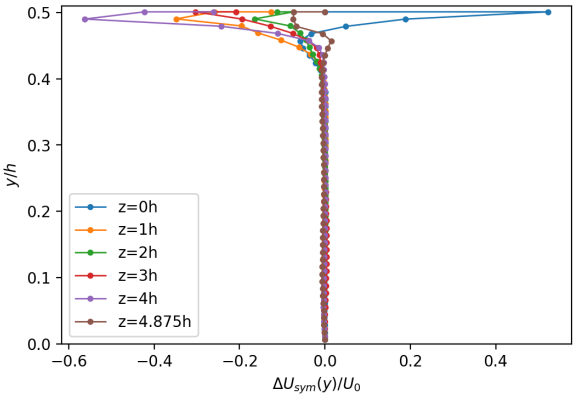

(b) Inverter frequency of 20 Hz.

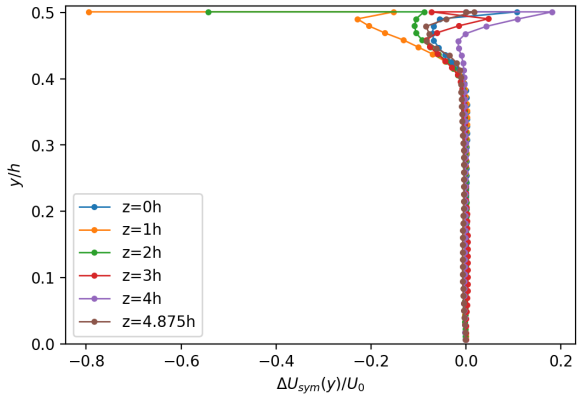

(c) Inverter frequency of 30 Hz.

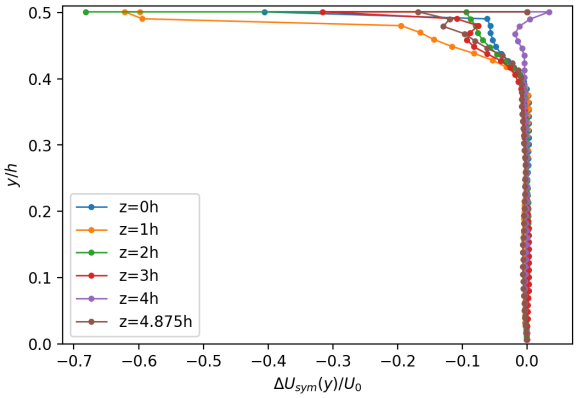

(d) Inverter frequency of 35 Hz.

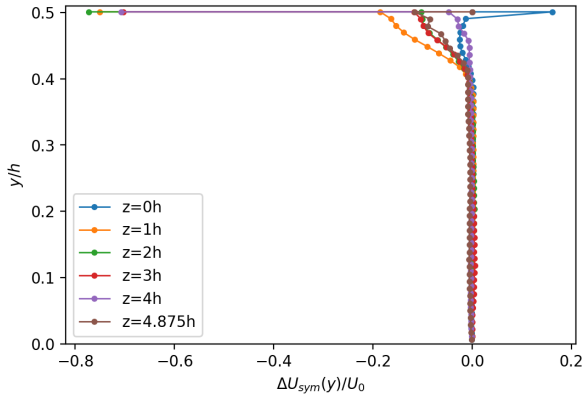

(e) Inverter frequency of 40 Hz.

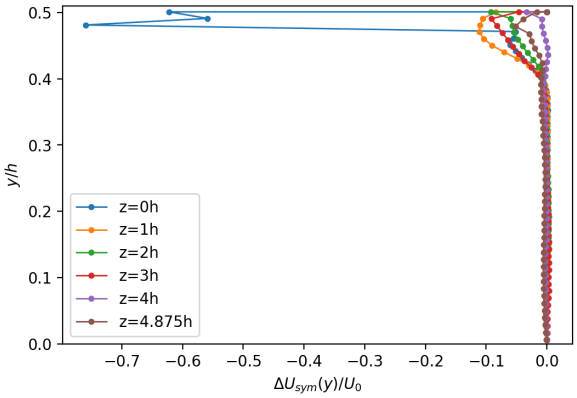

(f) Inverter frequency of 45 Hz.

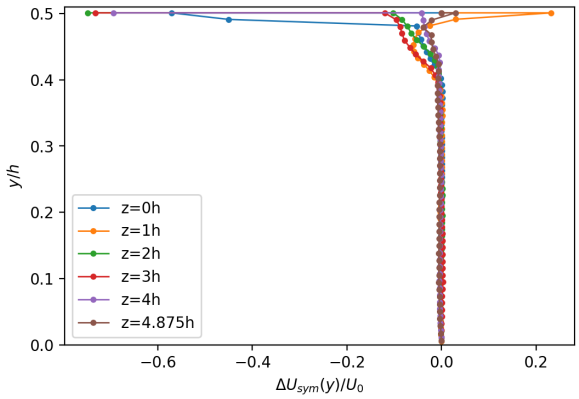

(g) Inverter frequency of 50 Hz.

Figure 7.0: Normalized differences between the upper and lower velocity profiles.

Another source that can influence the profiles' shape are the errors that can be present in the vector field due to noise in the PIV measurements. Indeed the biggest

differences are localized in the near-wall region. As can be seen in Fig.7.1 during image recording, strong reflections are evident along the boundaries of the channel.

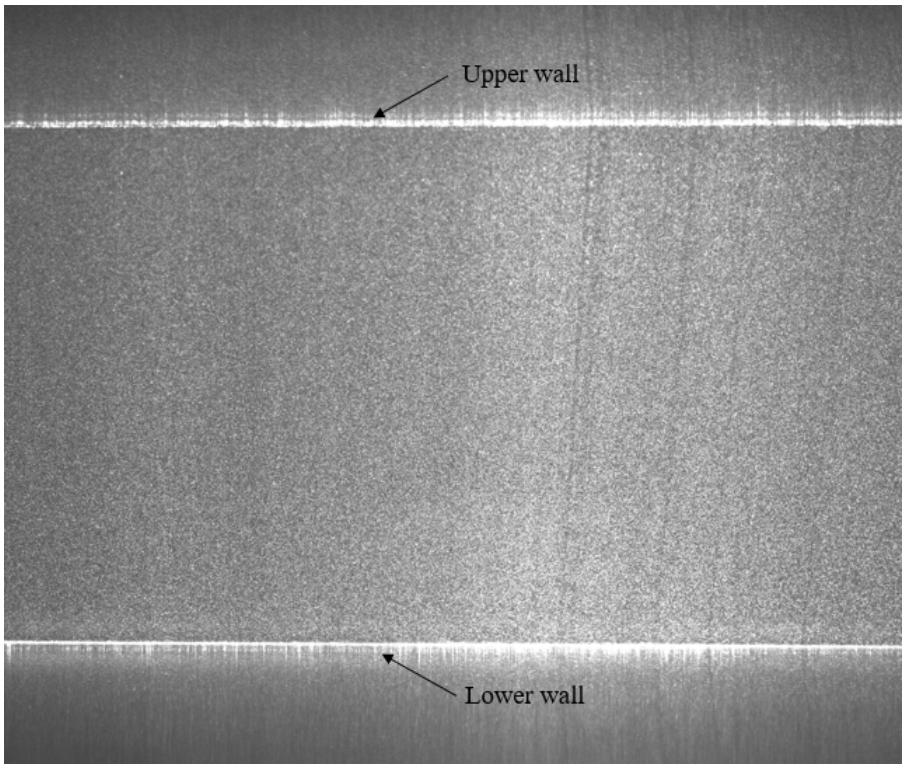

Figure 7.1: Example of full image taken from the image sequences used for the PIV analysis of the convergent; reflections can be seen along all the channel wall.

Regarding instead the spanwise profile in Fig.6.8, taken at the centerline with Pitot measurements, it reveals unexpected scatter of the mean value. At station -2.5δ and $+5\delta$, as velocity increases, the mean velocity reduces with respect to neighbour stations. This behaviour can be related to the PAT inlet. Indeed after the calm chamber, two tubes are used to connect it with the system of flow conditioners. The flow exiting from this ducts is not mixed because the directions of these flows is parallel and the center is approximately at $z = -6h$ and $z = +6h$. The previous configuration of the flow conditioner had a section made of three layers of marbles that indeed had the function of breaking up the flow exiting from the tubes and making it more uniform along the spanwise direction. For the present analysis, this section of marbles has been removed because it was introducing high pressure losses and the wind tunnel would have not reached the design working regime.

Moreover, the standard deviation variations along the spanwise stations are not showing any particular correlation. This suggests that convergence of the mean is verified along the spanwise direction and that the variations highlighted for the spanwise velocity profile are not due to statistical uncertainties only. The values are reported in Fig.7.2.

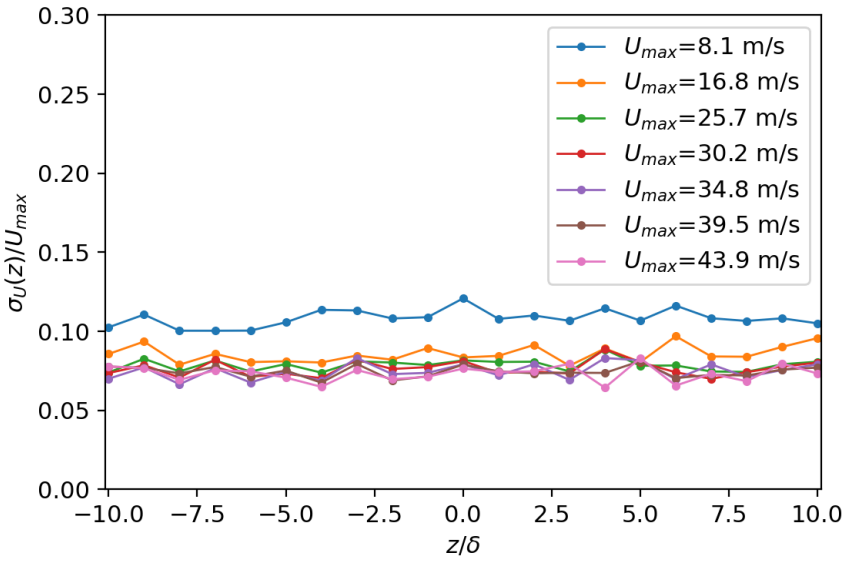

Figure 7.2: Standard devitations normalized with respect to maximum velocities, at different spanwise stations along the centerline.

Focusing now on the measurements carried out in the test section, despite the difference on the estimated δ_ν is $\sim 5\%$ and $\sim 11\%$ for u_τ, with respect to design conditions, the log law equation underestimates the velocity in the logarithmic region.

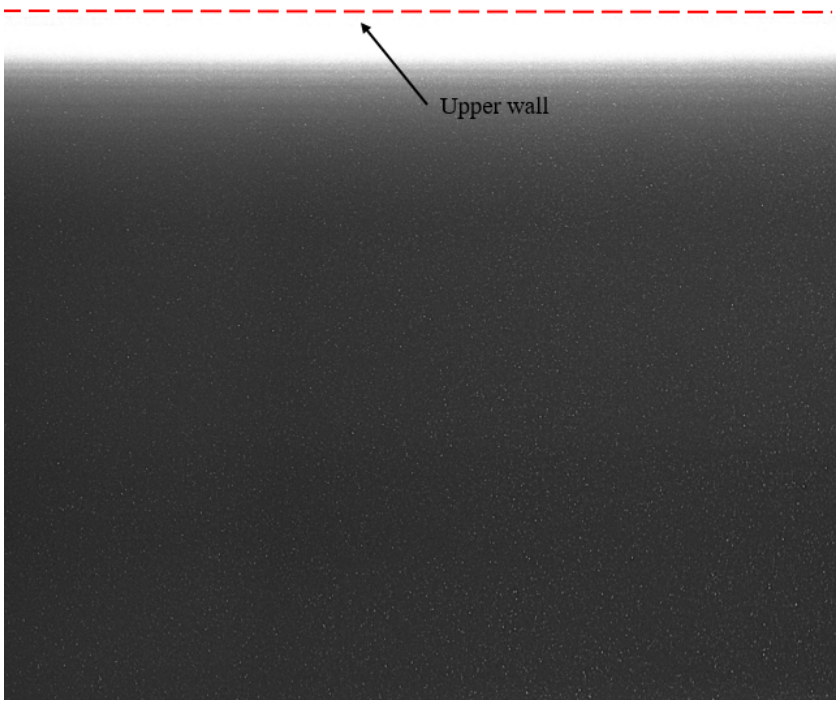

Figure 7.3: Example of full image taken from the image sequences used for the PIV analysis in the test section; red dashed line corresponds to the upper wall.

The values used for the log law constants are taken by [36] and even if the slope determined by k seems to replicate quite well the curve's slope in Fig.6.11, the constant B should be increased. Indeed in [20], [36] and [47] is reported that the scatter of k is around 5% with respect to the avarage value used and B can vary even from 4 to 6. Moreover should be pointed out the method used to estimate τ_w is affect by uncertainties since the scatter in $\tau(y)$ is quite high. To verify these results the only way is to estimate the inner scales via wall pressure measurements and compare the two solutions.

Moreover even if the spatial resolution is doubled with respect to previous analysis the results are affected by noise in the near wall region. Historical minimum of the image sequence has been computed and subtracted at all image pairs to remove background noise. This prepocessing did not improved at the end the sample and the percentage of invalid vectors remained around $3 - 4\%$. By looking at Fig.7.3 it is quite evident that the source of noise is mainly due again to reflexes. In this case the problem is further enhanced by the presence of the bright actuator surface.

Regarding plasma actuator tests, it is observed that for all the actuation modes, the x-component of velocity is reducing near wall compared to the not actuated case. Moreover, there is a prominent peak in v variance for the oscillating wall case at the lowest modulation frequency and all the actuated modes register an increase at the wall with respect to the base case. The peak of u variance as well as of the Reynolds stress are moved to higher y^+. All these effects of actuation reveal that this plasma actuator can influence the velocity field but further analysis are necessary to characterize the its behaviour. The present modes have been selected as first test case.

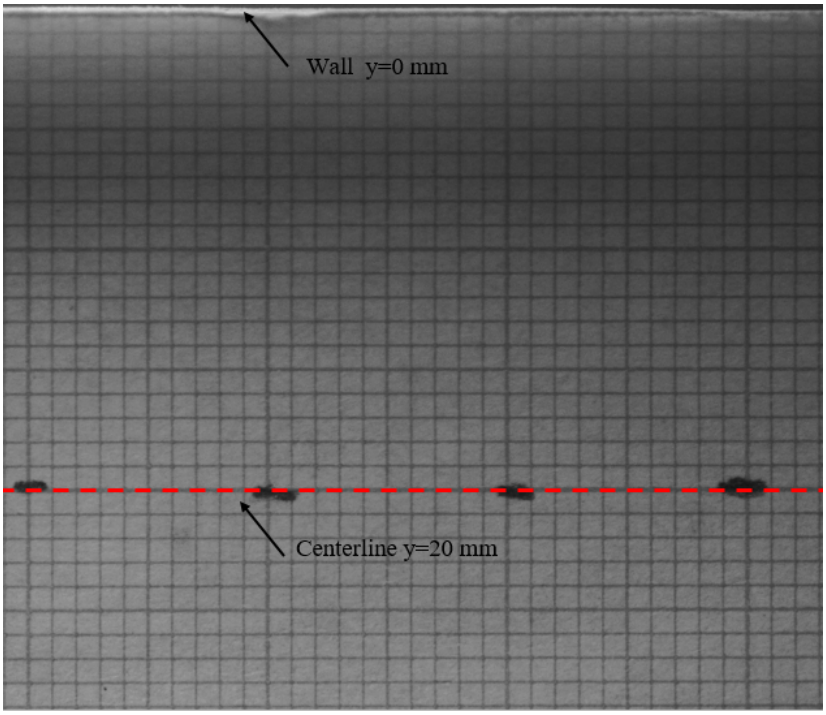

Figure 7.4: Image used for PIV analysis calibration; red dashed line, the channel's centerline used as reference for the coordinates system.

Moreover, regarding the estimation of the wall position, there is un uncertainty of the order of ± 4 *pixel*. This is due to the strategy used to define the origin of the coordinates reference system. It has been used a graph paper whose lines have an average width of 0.1 *mm* that corresponds to ~ 8 *pixel* according to the magnification used in the test section experiments. The wall position has been established as the first position close to 20 *mm* away from the centerline and the centerline location has been declared during calibration with the aforementioned uncertainty. Fig.7.4 shows the graph paper used as target for the calibration of the PIV magnification factor.

Chapter 8

Conclusions

The validation of the wind tunnel highlights that the velocity profiles, along the y direction, confirm to be top-hat for all the spanwise stations analysed; this is compliant with the design goal of a turbulent channel. However, the spanwise profile exhibits undesired scatter at stations -3δ and $+5\delta$ that could be due to the PAT inlet geometry (two separate tubes at the inlet of the flow conditioners). This effect increases as velocity increases. The velocity profile in inner units, at the mid-plane of the test section, appears to be in agreement with other test cases present in literature; the log law, with historical average values for k and B coefficients, is respected by the velocity profile in the expected log region when normalized with the inner scales δ_ν and u_τ found with the design procedure.

Even if the scope of this thesis is not analysing the effect of actuation modes on the flow, regarding the actuator used for this preliminary test, it can be concluded that at all the actuation modes tested yield a reduction in the x-component of the velocity especially near the wall.

The PIV analysis showed some problems in correctly reconstructing the velocity field very close to the wall, and this is evidently due to the strong reflections present along the walls. However, the field in the logarithmic layers has been resolved in a proper way.

8.1 Future works

Due to time constraints, it has not been possible to fully analyse the anomalies presented in the previous chapter, such as the symmetry discrepancies of the velocity profiles. Thus, as further tests for the validation of this platform, there are suggested:

- Analyse the evolution of the centerline vertical velocity profile along the streamwise direction: this will confirm if in the test section is valid the hypothesis of fully-developed flow;
- Add only one layer of marbles after the inlet of the flow conditioner in the PAT and repeat the analysis of the spanwise velocity profile at the centerline to verify if the scatter found during the present work is reduced;
- Add pressure ports at the wall in order to derive inner scales via wall pressure measurements to be compared with present results.

If the streamwise analysis will demonstrate that fully-developed condition is still not reached, thanks to the modularity of the wind tunnel, it is possible to add at any moment one or, if required, more additional sections.

On the other hand, for improving the PIV images, it is recommended to reduce further the laser intensity and increase seeding density, since it has been observed that the contribution of light emitted by plasma has a minimum effect. In this way, reflections will be reduced.

Even if in this present work are not available the results about power estimation via Lissajous curves technique, the algorithm for deriving the power consumed by the actuator has been implemented during this project. The algorithm computes its value directly from measurements of voltage of the acquisition system. Thus, it is only necessary to connect the proper capacitor to the actuator circuit and the power consumption can be readily estimated.

Bibliography

[1] Salem S. Abdel Aziz, Essam B. Moustafa, and Abdel-Halim Saber Salem Said. "Experimental Investigation of the Flow, Noise, and Vibration Effect on the Construction and Design of Low-Speed Wind Tunnel Structure". In: *Machines* 11.3 (2023). ISSN: 2075-1702. DOI: 10.3390/machines11030360. URL: https://www.mdpi.com/2075-1702/11/3/360.

[2] Md Abdullah et al. "Recent advancements in flow control using plasma actuators and plasma vortex generators". In: *Heat Transfer* 53 (July 2024), pp. 4244–4267. DOI: 10.1002/htj.23131.

[3] R.J. Adrian and J. Westerweel. *Particle Image Velocimetry*. Cambridge Aerospace Series. Cambridge University Press, 2011. ISBN: 9780521440080. URL: https://books.google.sm/books?id=jbDl2-yHbooC.

[4] Joint Institute for Aeronautics et al. *Contraction Design for Small Low-speed Wind Tunnels*. 1988. URL: https://books.google.sm/books?id=pvADAAAAIAAJ.

[5] Alex Alvisi. "Progettazione di un sistema di calibrazione ex-situ per anemometri a filo caldo". URL: https://amslaurea.unibo.it/id/eprint/16470/.

[6] Tommaso Astarita and Gennaro Cardone. "Analysis of interpolation schemes for image deformation methods in PIV". In: *Experiments in Fluids* 38 (Feb. 2005), pp. 233–243. DOI: 10.1007/s00348-004-0902-3.

[7] J.B. Barlow, W.H. Rae, and A. Pope. *Low-Speed Wind Tunnel Testing*. Wiley, 1999. ISBN: 9780471557746. URL: https://books.google.sm/books?id=nUHWDwAAQBAJ.

[8] Carlo Borghi et al. "Wind Tunnel Experiments on a NACA0015 Airfoil Equipped with Vectorizable Dielectric Barrier Discharge Plasma Actuators". In: June 2014. ISBN: 978-1-62410-288-2. DOI: 10.2514/6.2014-2684.

[9] Rodrigo Castellanos et al. "Reducing turbulent convective heat transfer with streamwise plasma vortex generators". In: *Experimental Thermal and Fluid Science* 134 (Jan. 2022), p. 110596. DOI: 10.1016/j.expthermflusci.2022.110596.

[10] Louis Cattafesta, Christopher Bahr, and Jose Mathew. "Fundamentals of Wind-Tunnel Design". In: Dec. 2010. ISBN: 9780470686652. DOI: 10.1002/9780470686652.eae532.

[11] Ning Hsing Chen. "An explicit equation for friction factor in pipe". In: *Industrial & Engineering Chemistry Fundamentals* 18.3 (1979), pp. 296–297.

[12] J. A. Clark. “A Study of Incompressible Turbulent Boundary Layers in Channel Flow”. In: *Journal of Basic Engineering* 90.4 (Dec. 1968), pp. 455–467. ISSN: 0021-9223. DOI: 10.1115/1.3605163. eprint: https://asmedigitalcollection.asme.org/fluidsengineering/article-pdf/90/4/455/5765083/455_1.pdf. URL: https://doi.org/10.1115/1.3605163.

[13] Geneviève Comte-Bellot and Antoine Craya. *Écoulement turbulent entre deux parois parallèles*. Publications scientifiques et techniques du Ministère de l'air. Service de documentation scientifique et technique de l'armement, 1965, 159 p. URL: https://hal.science/hal-00567117.

[14] Thomas Corke, C. Enloe, and Stephen Wilkinson. “Dielectric Barrier Discharge Plasma Actuators for Flow Control*”. In: *Annual Review of Fluid Mechanics* 42 (Dec. 2009), pp. 505–529. DOI: 10.1146/annurev-fluid-121108-145550.

[15] Andrea Cristofolini, Carlo A. Borghi, and Gabriele Neretti. “Charge distribution on the surface of a dielectric barrier discharge actuator for the fluid-dynamic control”. In: *Journal of Applied Physics* 113.14 (Apr. 2013), p. 143307. ISSN: 0021-8979. DOI: 10.1063/1.4799159. eprint: https://pubs.aip.org/aip/jap/article-pdf/doi/10.1063/1.4799159/13210743/143307_1_online.pdf. URL: https://doi.org/10.1063/1.4799159.

[16] S. Discetti and A. Ianiro. *Experimental Aerodynamics*. CRC Press, 2017. ISBN: 9781498704014. URL: https://books.google.sm/books?id=Cz9njwEACAAJ.

[17] C. Enloe et al. “Mechanisms and Responses of a Single Dielectric Barrier Plasma Actuator: Geometric Efiects”. In: *AIAA Journal* 42 (Mar. 2004).

[18] Luca Franceschelli. “Anemometri a filo caldo: studio e progettazione di un sistema di calibrazione”. URL: https://amslaurea.unibo.it/id/eprint/16544/.

[19] Sven Grundmann and Cameron Tropea. “Active cancellation of artificially introduced Tollmien–Schlichting waves using plasma actuators”. In: *Experiments in Fluids* 44 (May 2008), pp. 795–806. DOI: 10.1007/s00348-007-0436-6.

[20] A. K. M. F. Hussain and W. C. Reynolds. “Measurements in Fully Developed Turbulent Channel Flow”. In: *Journal of Fluids Engineering* 97.4 (Dec. 1975), pp. 568–578. ISSN: 0098-2202. DOI: 10.1115/1.3448125. eprint: https://asmedigitalcollection.asme.org/fluidsengineering/article-pdf/97/4/568/5631445/568_1.pdf. URL: https://doi.org/10.1115/1.3448125.

[21] I.E. Idel'chik and M.O. Steinberg. *Handbook of Hydraulic Resistance*. Begell House, 1996. ISBN: 9781567000740. URL: https://books.google.sm/books?id=Fvh6i4TipsgC.

[22] Romain Joussot et al. “Plasma morphology and induced airflow characterization of a DBD actuator with serrated electrode”. In: *Journal of Physics D: Applied Physics* 46 (Feb. 2013), p. 125204. DOI: 10.1088/0022-3727/46/12/125204.

[23] Burak Karadag, Cem Kolbakir, and Ahmet Selim Durna. “Plasma actuation effect on a NACA 4412 airfoil”. In: *Aircraft Engineering and Aerospace Technology* (Aug. 2021). DOI: 10.1108/AEAT-04-2021-0101.

[24] K V Karthikeyan and R Harish. “Advancements in flow control using plasma actuators: a comprehensive review”. In: *Engineering Research Express* 7.1 (Jan. 2025), p. 012502. DOI: 10.1088/2631-8695/adabb3. URL: https://dx.doi.org/10.1088/2631-8695/adabb3.

[25] Ulrich Kogelschatz. “Filamentary, Patterned, and Diffuse Barrier Discharges”. In: *Plasma Science, IEEE Transactions on* 30 (Sept. 2002), pp. 1400–1408. DOI: 10.1109/TPS.2002.804201.

[26] Marios Kotsonis. “Diagnostics for characterisation of plasma actuators”. In: *Measurement Science and Technology* 26.9 (Aug. 2015), p. 092001. DOI: 10.1088/0957-0233/26/9/092001. URL: https://dx.doi.org/10.1088/0957-0233/26/9/092001.

[27] Jochen Kriegseis et al. “Capacitance and power consumption quantification of dielectric barrier discharge (DBD) plasma actuators”. In: *Journal of Electrostatics - J ELECTROSTAT* 69 (Aug. 2011), pp. 302–312. DOI: 10.1016/j.elstat.2011.04.007.

[28] Jochen Kriegseis et al. “PIV-based Estimation of DBD Plasma-Actuator Force terms”. In: Jan. 2012. DOI: 10.2514/6.2012-411.

[29] John. Laufer. “Investigation of Turbulent Flow in a Two-Dimensional Channel”. In: (1951).

[30] Ying-hong Li et al. “Plasma Flow Control”. In: *Aeronautics and Astronautics*. Ed. by Max Mulder. Rijeka: IntechOpen, 2011. Chap. 2. DOI: 10.5772/17935. URL: https://doi.org/10.5772/17935.

[31] Kim Lien et al. “The entrance length for fully developed turbulent channel flow”. In: *15th Australian fluid mechanics conference*. Vol. 15. University of Sydney, Sydney, Australia. 2004, pp. 356–363.

[32] Björn Lindgren and Arne Johansson. “Design and Evaluation of a Low-Speed Wind-Tunnel with Expanding Corners”. In: (Jan. 2002).

[33] R.D. Mehta. “The aerodynamic design of blower tunnels with wide-angle diffusers”. In: *Progress in Aerospace Sciences* 18 (1979), pp. 59–120. ISSN: 0376-0421. DOI: https://doi.org/10.1016/0376-0421(77)90003-3. URL: https://www.sciencedirect.com/science/article/pii/0376042177900033.

[34] R.D. Mehta and P. Bradshaw. “Design rules for small low speed wind tunnels”. In: *The Aeronautical Journal* 83 (July 2016), pp. 443–453. DOI: 10.1017/S0001924000031985.

[35] Gabriele Neretti. “Active Flow Control by Using Plasma Actuators”. In: *Recent Progress in Some Aircraft Technologies*. Ed. by Ramesh K. Agarwal. Rijeka: IntechOpen, 2016. Chap. 3. DOI: 10.5772/62720. URL: https://doi.org/10.5772/62720.

[36] S.B. Pope. *Turbulent Flows*. Cambridge University Press, 2000. ISBN: 9780521598866. URL: https://books.google.sm/books?id=HZsTw9SMx-0C.

[37] M. Raffel et al. *Particle Image Velocimetry: A Practical Guide*. Experimental Fluid Mechanics. Springer Berlin Heidelberg, 2007. ISBN: 9783540723073. URL: https://books.google.sm/books?id=WH5w2TvK2bQC.

[38] Frederico Rodrigues, José Páscoa, and Michele Trancossi. “Plasma Actuators Optimization Using Stair Shaped Dielectric Layers”. In: Nov. 2019. DOI: 10.1115/IMECE2019-11515.

[39] D. V. Roupassov et al. “Flow Separation Control by Plasma Actuator with Nanosecond Pulsed-Periodic Discharge”. In: *AIAA Journal* 47.1 (2009), pp. 168–185. DOI: 10.2514/1.38113. eprint: https://doi.org/10.2514/1.38113. URL: https://doi.org/10.2514/1.38113.

[40] Fulvio Scarano. “Iterative image deformation methods in PIV”. In: *Measurement Science and Technology* 13 (Nov. 2001), R1. DOI: 10.1088/0957-0233/13/1/201.

[41] Kazuo Shimizu, Yoshinori Mizuno, and Marius Blajan. “Basic Study on Flow Control by Using Plasma Actuator”. In: *IEEE Transactions on Industry Applications* 51.4 (2015), pp. 3472–3478. DOI: 10.1109/TIA.2015.2397174.

[42] Jin-Jun Wang et al. “Recent developments in DBD plasma flow control”. In: *Progress in Aerospace Sciences* 62 (2013), pp. 52–78. ISSN: 0376-0421. DOI: https://doi.org/10.1016/j.paerosci.2013.05.003. URL: https://www.sciencedirect.com/science/article/pii/S0376042113000535.

[43] Jinjun Wang and Lihao Feng. “Plasma Actuator”. In: *Flow Control Techniques and Applications*. Cambridge Aerospace Series. Cambridge University Press, 2018, pp. 206–245.

[44] Wu et al. “Experimental investigation of nanosecond discharge plasma aerodynamic actuation”. In: *Chinese Physics B* 21.4 (Apr. 2012). DOI: 10.1088/1674-1056/21/4/045202.

[45] Zhenyu Xue, John J Charonko, and Pavlos P Vlachos. “Particle image velocimetry correlation signal-to-noise ratio metrics and measurement uncertainty quantification”. In: *Measurement Science and Technology* 25.11 (2014), p. 115301. DOI: 10.1088/0957-0233/25/11/115301. URL: http://dx.doi.org/10.1088/0957-0233/25/11/115301.

[46] L. Yue et al. “Effect of Plasma Actuator on Flow Field”. In: *Acta Physica Polonica A* (2022). URL: https://api.semanticscholar.org/CorpusID:246793995.

[47] E.-S. Zanoun, F. Durst, and H. Nagib. “Evaluating the law of the wall in two-dimensional fully developed turbulent channel flows”. In: *Physics of Fluids* 15.10 (Oct. 2003), pp. 3079–3089. ISSN: 1070-6631. DOI: 10.1063/1.1608010. eprint: https://pubs.aip.org/aip/pof/article-pdf/15/10/3079/19131388/3079_1_online.pdf. URL: https://doi.org/10.1063/1.1608010.